



Review

Additive Manufacturing of Aluminum Alloys for Aeronautic Applications: Advantages and Problems

Roberto Montanari * , Alessandra Palombi, Maria Richetta  and Alessandra Varone

Department of Industrial Engineering, University of Rome "Tor Vergata", 00133 Rome, Italy

* Correspondence: roberto.montanari@uniroma2.it; Tel.: +39-06-7259-7182

Abstract: In aeronautics, additive manufacturing (AM) leads to specific benefits, mainly connected to topological optimization for weight reduction, the decrease in "buy-to-fly" ratio, and the operations of maintenance, repair, and overhaul. Al alloys processed by AM technologies are extensively investigated and play an increasing role in the production of aircraft structural parts. Based on the recent literature and research activity of the authors, this work examines advantages and drawbacks involved in the printing of Al alloys. Defects, microstructure, mechanical properties, development of new alloys, and postprocess treatments are described and critically discussed by focusing the attention on the effects of the specific alloy composition, AM process, and process parameters.

Keywords: Al alloys; additive manufacturing; aeronautics; defects; microstructure; mechanical properties



Citation: Montanari, R.; Palombi, A.; Richetta, M.; Varone, A. Additive Manufacturing of Aluminum Alloys for Aeronautic Applications: Advantages and Problems. *Metals* **2023**, *13*, 716. <https://doi.org/10.3390/met13040716>

Academic Editors: Alexander M. Korsunsky, Atef Saad Hamada and Alexey I. Salimon

Received: 20 February 2023

Revised: 20 March 2023

Accepted: 31 March 2023

Published: 5 April 2023



Copyright: © 2023 by the authors. Licensee MDPI, Basel, Switzerland. This article is an open access article distributed under the terms and conditions of the Creative Commons Attribution (CC BY) license (<https://creativecommons.org/licenses/by/4.0/>).

1. Introduction

The development of new materials with improved characteristics is one of the key factors for producing aircrafts with reduced operating costs [1]. The target is the extension of aircraft service life combined with greater fuel efficiency to achieve an increase in payload and flight range. The challenge consists in reducing the weight of structures and components by using materials which at the same time guarantee better corrosion resistance and mechanical properties, in particular damage tolerance, fatigue, and wear behavior [2,3].

In a previous paper [4], the specific conditions (stress, geometric limits, environment, production, maintenance, etc.) leading to the choice of the material for structural applications in transport aircraft were described. In general, the main requirements are low density for reducing the weight and suitable mechanical properties for bearing the static weight of the aircraft and the additional loads related to flight turbulence and specific maneuvers, such as taxiing, take-off, and landing. In addition, owing to the extreme conditions of temperature and humidity, the structural alloys must exhibit a good corrosion resistance.

Although composites play an increasing role as aeronautic structural materials, Al alloys still represent materials of fundamental importance, and among the lightweight alloys, they are the most used, owing to their good workability and low cost.

In the last years, additive manufacturing (AM) has gained importance in different industrial areas, and several alloys can be manufactured by using this innovative technology. In aeronautics, AM involves specific benefits, mainly connected to: (i) the application of topological optimization (TO) for weight reduction and improved efficiency, (ii) the decrease in "buy-to-fly" ratio that reduces waste material and contributes to lower manufacturing costs, and (iii) the optimization of maintenance, repair, and overhaul (MRO) operations to reduce costs associated with downtime [5]. MRO includes inspection, replacement of damaged parts, refilling of gases and lubricants, coating fixing, etc., and it is strictly regulated by aeronautical national and international authorities due to its relevance for safety. Indeed, MRO assures that every time an aircraft flies, it is compliant with the airworthiness directives.

A way to reduce the weight of aircraft components consists in integrating TO criteria in the design and fabrication processes of structural components. TO determines the minimum amount of mass and its optimal distribution on a certain part under specific conditions of applied loads (e.g., see [6–8]); thus, it is more flexible and efficient than the use of materials such as metallic foams [9–11]. In addition to the development of greater computational power, more sophisticated software, and an increased integration of robotics in machining processes, TO strictly requires novel manufacturing technologies. AM meets such needs quite well, allowing to manufacture components of complex geometry without joints, reduce the mass, incorporate internal features, and use novel alloy compositions. Lattice structures, which imitate trabecular features typical of animal and human bones, wood, leaves, and other natural structures, can guarantee a high degree of efficiency with consequent advantages in reducing weight, material, energy in transportation, and pollution emissions. Therefore, the main companies of the aircraft industry have been exploring the possibility to produce aircraft components through AM, such as interior parts, brackets, and hinges, as well as fuselages and airframes of lighter weight; some recent applications are reported in Section 2. AM applications are also related to the engines: integrated piping systems, compressors, fuel nozzles, and turbine blades with internal cooling channels [12–14].

Another aspect that makes this technology of great interest for aeronautics is related to the reduction in the “buy-to-fly” ratio, i.e., the mass of raw material needed per unit mass of finished component. Today, the ratio is in the range 12–25 for aircraft components made of Al alloys and manufactured through conventional processes, resulting in large amounts of materials scrap in the cradle-to-gate manufacturing system. This involves high manufacturing costs and large environmental emissions footprints. For example, a recent study by Huang et al. [15] estimated the environmental benefits of a shift from conventional to AM of lightweight metallic aircraft components through the year 2050 in the U.S. aircraft industry: fleetwide lifecycle primary energy savings reach 70–173 million GJ/year in 2050, with cumulative savings of 1.2–2.8 billion GJ. Therefore, there is an increasing interest of aircraft industries to develop and deploy AM components.

Finally, AM is quite promising for aeronautic MRO operations: the purpose is to speed up the replacement of components and reduce costs associated with inventory and transportation [16]. AM allows just-in-time production based on digital data and replacement of mechanical parts through relatively simple machinery and, in short, manufacturing time. For example, by using AM instead of traditional manufacturing, a helicopter rotor blade has been produced by ACS in 2 days instead of 45 days, with a cost reduction of USD 1588 [17]. Therefore, the appropriate integration of AM technology with the aeronautic industry could lead to great benefits to the supply chain, even if the lack of quality assurance and certification standards still represent obstacles to significant advancements in this direction [5].

AM drawbacks are mainly related to surface roughness, porosity, residual stress, cracks, unique microstructures, and material anisotropy; therefore, postprocessing is required with custom-developed thermomechanical treatments, surface polishing and, in some cases, final machining. The quality of components and their mechanical properties strongly depend on the complexity of the process; thus, controversial data are found in the literature (e.g., see [18–21]). Given some uncertainties in the microstructure and performance of AM parts, the controls must be different from the traditional ones, and new international standards and procedures are currently under development [22]. Finally, it must be considered that today, AM technology is not yet as readily available as traditional techniques. The last updates on AM technologies and their main applications in the aviation industry have been reviewed in a recent paper by Gisario et al. [23].

In spite of these obstacles in the use of AM technology on a large scale in aeronautics, its possible role in relaxing the pressures in the supply chain system of the aircraft industry is a topic of great interest.

In recent years, several papers have been published on this topic, and there are many reviews focused on different aspects, such as specific type of material, technology, application, etc. For instance, an excellent review paper on the AM of Al alloys is that of Kotadia et al. [24]. The present work focuses its attention on opportunities and specific problems connected to the application of printed Al alloys in aeronautics. On the basis of the recent literature and research activity of the authors, the advantages and drawbacks involved in the AM of structural aircraft components made of Al alloys are examined. Section 2 presents some applications in aeronautics of Al alloys, while Sections 3–5 are devoted to the defects present in printed components, microstructures and mechanical properties, and postprocess treatments, respectively. Al alloys prepared by AM exhibit some common defects and microstructural characteristics, which are described and discussed by focusing the attention on the effects of specific composition of the alloys, AM process, and process parameters. Section 6 highlights the problems involved in postprocess treatments, which are carried out to minimize the defects and improve the microstructural features, and it considers some possible solutions.

The scope of the work is to present the state of the art and indicate some points of particular interest for future work.

2. Applications of AM Parts Made of Al Alloys

Al alloys are largely used to manufacture structural components for the aeronautic industry due to their high specific mechanical properties and good corrosion resistance. Although AM could replace conventional manufacturing with significant advantages, the applications of printed Al alloy are still limited by the difficulty to meet the high aeronautic standards, especially for structural components. Moreover, while traditional technologies have been investigated for years, the research on AM is quite young; thus, there are high costs for quality inspection [25]. Collecting data on properties of printed materials can reduce qualification costs and help to develop specific standards for this method. Today, standards on the characteristics of feedstock material, allowable defects, and inspection methods do exist; however, others regarding surface finish and damage tolerance should be developed or improved [26].

The first use of AM components in aeronautics dates back to 2014, when Airbus installed a cabin bracket connector made of Ti6Al4V on a commercial A350 aircraft, designed by TO and manufactured by Laser Powder Bed Fusion (L-PBF) [27]. Since then, AM entered rapidly in the design and production systems of aeronautic industry. In 2017, structural Ti6Al4V components produced by Direct Energy Deposition (DED) were installed on the Boeing 787 Dreamliner [28]. In the same year, Airbus started the serial production of a 3D-printed pylon bracket in Ti alloy for the A350 XWB aircraft, namely a critical component that is part of the pylon joining engine and wing [29], and GKN Aerospace Engine Systems announced to have started research on AM applications for aircraft components [30]. Other components for aircraft interiors were developed by Airbus, e.g., a Ti6Al4V door locking shaft [31], an aircraft lattice seat made of Mg and designed by TO [32], and a borescope boss for A320neo, which is an access point for inspecting turbines [31].

Among light alloys printed by AM technologies, those of Al play a dominant role; some significant examples are reported in the following.

A lattice partition wall made of AlMgSc, namely a thin panel separating the seats from the plane galley of A320 aircraft, is shown in Figure 1 [33]. They calculated that the lattice structure of the partition wall led to a reduction in the total weight of about 30 Kg, with an estimated CO₂ emission saving of 465,000 metric tons every year.

The combined advantages of AM and TO allow the manufacturing of structural components with high mechanical properties and a considerably lower mass than the original ones. Two significant examples are given in Figure 2.

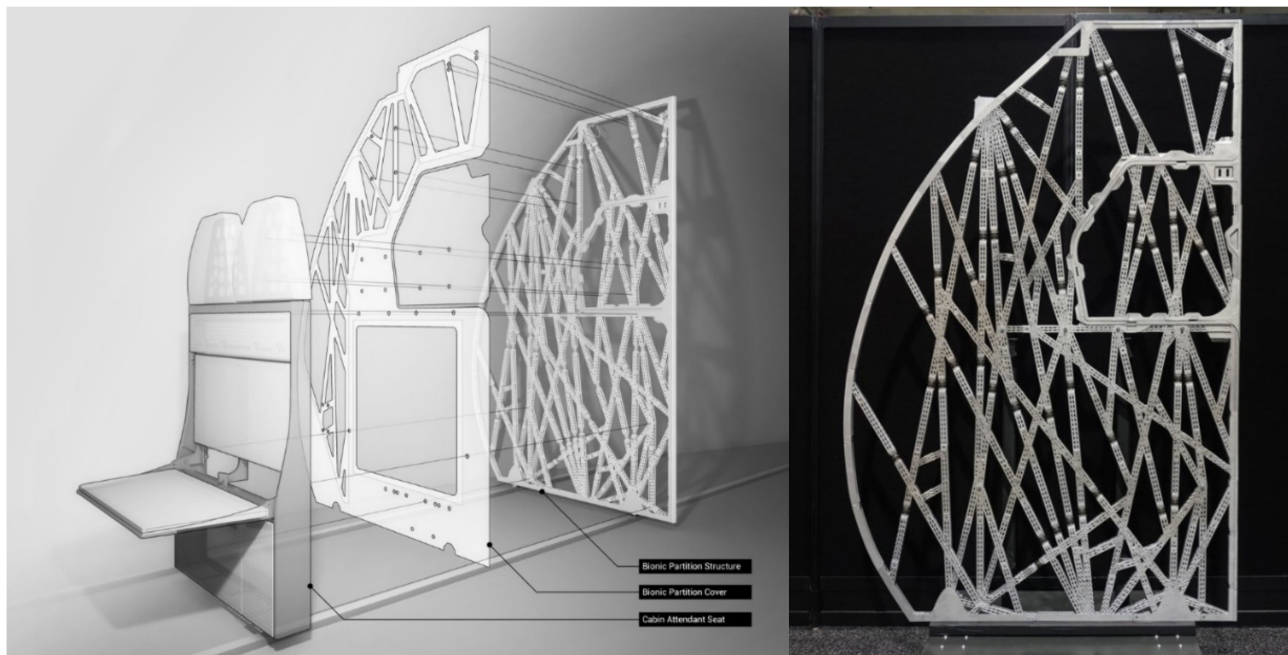


Figure 1. Airbus lattice structure of a partition wall made of AlMgSc alloy and produced by L-PBF [33] (image courtesy of The Living).



(a)



(b)

Figure 2. EOS and RUAG antenna bracket made of AlSi10Mg and manufactured by L-PBF (a) [34] (Image taken from <https://www.eos.info/en/academic-info> (accessed on 28 March 2023), Source: EOS GmbH); brackets mounted on Boeing 787 (b) [35] (Image courtesy of Spirit Aerosystems and provided for an article by Additive Manufacturing Media: <https://www.additivemanufacturing.media/articles/what-is-the-role-for-additive-manufacturing-in-aircraft-structural-components> (accessed on 28 March 2023)).

Figure 2a shows an AlSi10Mg antenna bracket manufactured by L-PBF; the original component was redesigned to obtain a weight reduction of 40% [34]. Similarly, EOS and Sogeti managed to produce a vertical tail plane bracket in a shorter time with a 30% mass reduction and in one single part, while the original one was made of more than 30 parts,

both metallic and plastic [36]. A bracket mounted on a Boeing 787 [35] is displayed in Figure 2b; such components are quite common today in aircrafts due to the lower costs linked to reduced material waste and production time. The cost reduction linked to AM of aircraft components is one of the key factors driving the aeronautic industry towards these technologies [37].

Al alloys have also been employed in the AM of lattice structured cooling systems of combustion engines. One example is the AlSi10Mg microturbine generator housing manufactured by nTopology and Cobra Aero (Figure 3a,b) [38]. The manufacturers showed a 50% reduction in waste material and the possibility to produce the system in one single component, instead of the six parts required in traditional manufacturing.

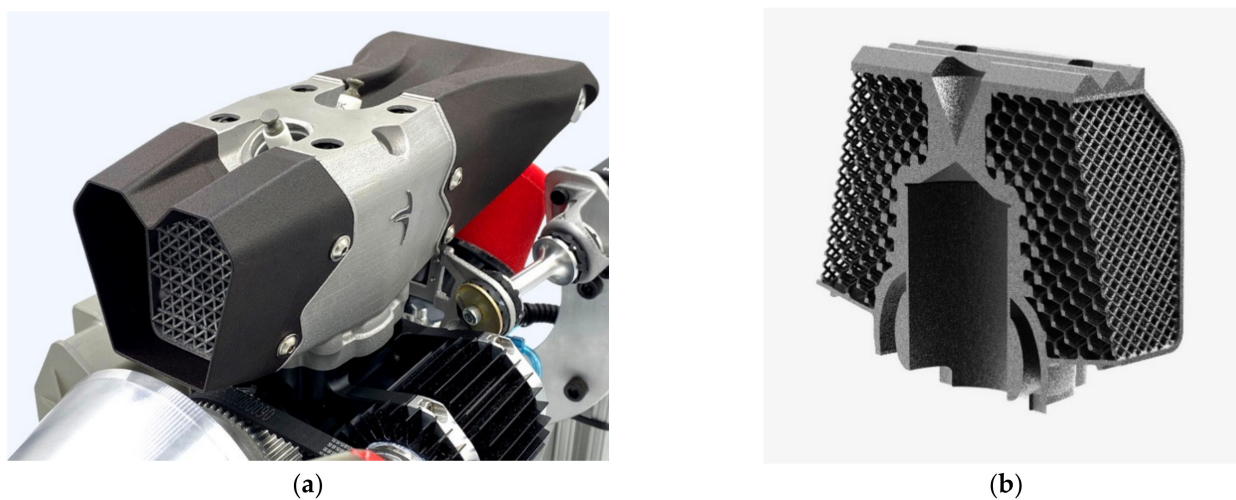


Figure 3. Microturbine generator housing (a); cross-section of the cooling system of the combustion engine cylinder (b) [38] (image courtesy of nTopology).

The reported applications show the great progress which allowed the passage of AM from lab to production, although it is not yet a mature technology. Since the quality of aeronautic components is subjected to strict requirements, production on large industrial scale through AM technologies is hindered by uncertainties in material performance. The building up of components layer by layer to a final shape from a 3D model created using Computer-Aided Design (CAD) is a complex procedure, and a multitude of process parameters may affect the final quality of the products. In the next section, the main defects which are present in printed Al alloys and determine their properties are examined. Understanding the origin of defects in the production process and the specific role played by process parameters is fundamental to optimize procedures, enhance the quality of components, and open the way for a more extended use of AM in aeronautics.

3. Defects

AM technology offers the opportunity of modified or novel compositions to obtain builds of high strength without defects such as cracks, often observed in conventional alloys [39–42]. Moreover, components of complex geometry without joints, reduced mass, and incorporating internal features can be produced [43], and this represents a great advantage in the use of Al and its alloys in aeronautic applications. However, these materials exhibit some drawbacks, such as high thermal conductivity and high reflectivity in the laser wavelength range used in some common AM processes [44,45]. The combination of high-power laser beams and low scan speeds employed to compensate for heat dissipation leads to large melt pools, balling, damage to the powder distribution system, and relevant impact on printing time and costs [46]. For instance, the Selective Laser Melting (SLM) process of Al requires a laser power of at least 150 W at a scan speed of 50 mm/s to achieve densities close to 100% for a layer thickness of 50 μm . A possible solution has been

described by Buchbinder et al. [47], who investigated the improvement of SLM performance by increased laser power up to 1 kW.

Another drawback is the high susceptibility of Al alloys to oxidation: oxides originally present on the powder and forming during AM processes cause a high degree of porosity in the final products. High porosity and poor surface quality hinder the application of these materials in components where fatigue resistance is a critical issue [48].

Due to the special processing conditions of AM, alloys in the AM field face problems such as inhomogeneous microstructure, excessive thermal residual stresses, and chemical composition adjustment. The main defects observed in Al components prepared by AM are (i) porosity; (ii) hot cracking, (iii) anisotropy, (iv) poor surface quality, and (v) residual stresses. These aspects are examined in the following subsections.

3.1. Porosity

Components made of Al alloys and manufactured by AM always exhibit a certain degree of porosity. The elimination of porosity is a challenging task, because it is related to both material composition and process parameters (see Figure 4); thus, the optimization of the characteristics of printed components involves the trade-off of different factors.

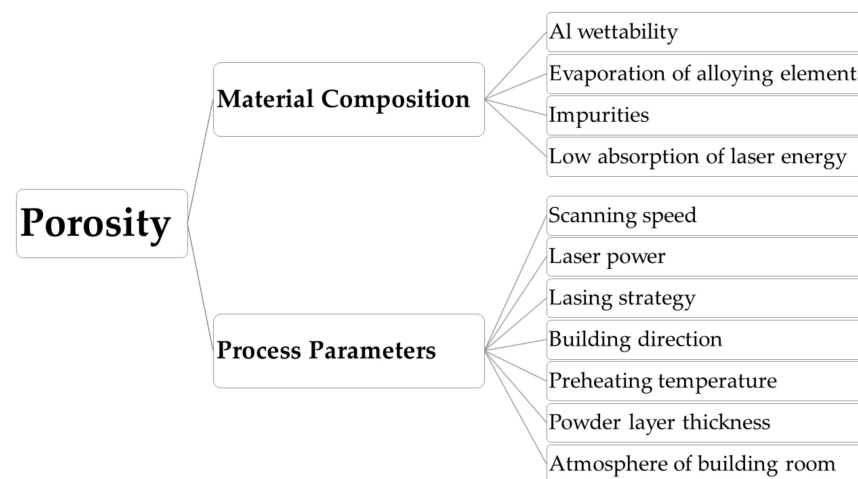


Figure 4. Causes of porosity in the AM process of Al alloys.

Material properties such as wettability, evaporation of alloying elements, presence of impurities in the liquid pool, and absorptivity of laser beam directly depend on the alloy composition. The manufacturing of a part by L-PBF can be considered as the movement of a melt pool across the surface, with powder at the front of the pool and solidified material at the back. The underlying and surrounding solid partially remelts, so that these regions are wet and fuse with the melt pool. In the case of Al alloys, an adherent solid oxide layer forms on the underlying solid and on the melt pool; thus, the wetting and fusing of Al regions is controlled by the disruption of these oxides, not by the melting of the different regions.

A mechanism describing the way oxide layers affect the formation of pores during L-PBF process has been proposed by Louvis et al. [46]: the heat source induces the evaporation of oxides on the upper surface of the melt pool, and Marangoni motions disrupt oxide layers on the lower surface, whereas oxides formed at the side of the melt pool are scarcely affected. As schematically shown in Figure 5, the remaining thin oxide fragments may trap gas and unmolten powder particles as the melt pool fails to wet the surrounding material. The major confounding factor for processing Al alloys is identified in the oxidation due to the presence of O within the build chamber, and they concluded that to produce 100% dense Al components by L-PBF, it is necessary to develop methods either to disrupt these oxide films or avoid their formation.

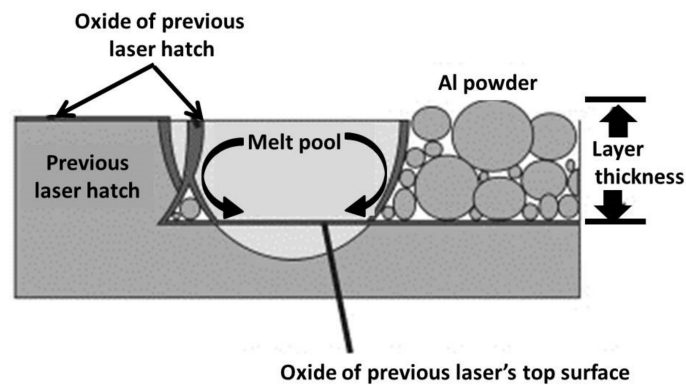


Figure 5. Thin oxide fragments trap gas and unmolten powder particles forming pores (redrawn from ref. [46]).

The control of the atmosphere in the build chamber is fundamental to reduce oxidation and porosity during solidification [48] and improve the final quality of components [49]. Elements with an evaporation temperature lower than the melting temperature of the alloy can evaporate during the process, resulting in a final product with a composition that is different from that of precursors [50]. Of course, this affects the wettability of liquid metal and may contribute to increase the porosity.

Generally, Al and Al alloys have a low laser absorptivity that may induce an incomplete melting of powders and finally lead to defects in the printed component. To overcome this problem, apart from a suitable tailoring of the alloy composition (e.g., elements such as Si and Mg enhance the absorptivity), an increase in energy density seems to be of help [51]. Energy density E_d (J/mm^3) can be expressed as

$$E_d = \frac{P}{v \cdot s \cdot t} \quad (1)$$

where P (W) is laser power, v (mm/s) scan speed, s (mm) scan spacing, and t (mm) layer thickness. By investigating AlSi7Mg0.3, Kimura and Nakamoto [52] observed that there is a critical value of the energy density to obtain components with optimal density (see Figure 6a).

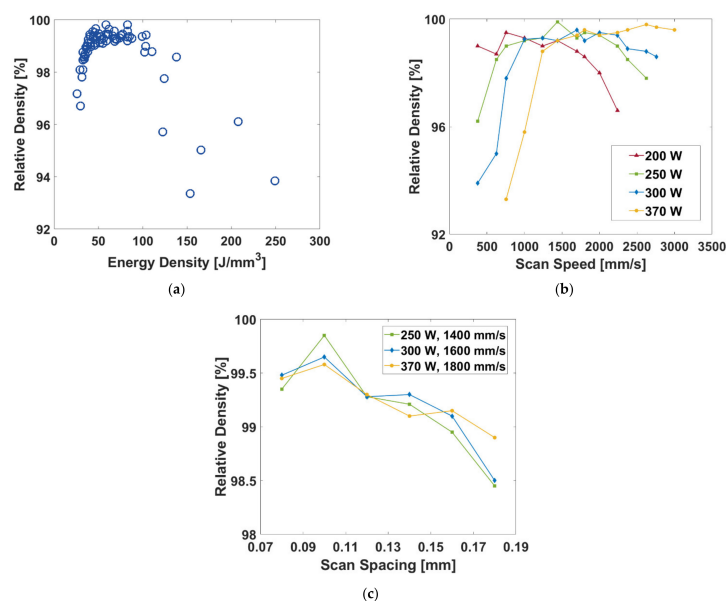


Figure 6. Influence of energy density (a), scan speed (b), and scan spacing (c) on the relative density of AlSi7Mg0.3 printed by L-PBF. Redrawn from ref. [52].

Below such a critical value (low-energy density), the material exhibits an incomplete melting of the powder layer, and some porosities remain as a matter of course, while above it (high-energy density), there are a lot of spherical gas pores. The layer thickness being constant, at a given laser power the energy density depends on scan speed v and scan spacing s ; thus, the right combination of these parameters allows to obtain the optimal value of energy density and consequently of density of manufactured components. Figure 6b,c shows the relative density of components obtained with different laser power by varying the scan speed and scan spacing, respectively. Similar results were obtained by Read et al. [53] by studying the AlSi10Mg alloy.

The effect of energy density on size, orientation, and distribution of the pores is evident by considering the scan strategy. Damon et al. [54] observed a higher density of clustered pores (200–300 μm) near the surface in AlSi10Mg components built by adopting the contour-core scan strategy, while larger pores near the preheated printing platform were detected by Cerri et al. [55]. These results evidence how the scan strategy may lead to variations of laser energy density in different parts of a single component with the result of inhomogeneous pore size and distribution.

Laser energy density controls the local heating; however, porosity also strongly depends on the cooling rate, because the higher the rate, the greater the amount of gas trapped in the solidified metal. This was clearly demonstrated by Hauser et al. [56], who investigated the correlation between porosity and shielding gas flow rate in Wire Arc Additive Manufacturing (WAAM). Since a high flow rate improves heat dissipation, rapid solidification occurs, and the gas remains trapped in the solid, causing higher porosity.

Different types of pores are found in printed parts depending on the scan speed v . Indeed, for each alloy, there is a critical scan speed (v_c): if $v < v_c$, metallurgical pores are observed, whereas if $v > v_c$, keyhole pores are observed [57]. The overall porosity does not depend only on scan speed but also on laser power and scan spacing. Scan speed and laser power are interconnected, and their influence can be evaluated by considering the energy density. Generally, high energy density reduces porosity and leads to higher hardness values; however, high scan speeds promote the spattering phenomenon [58].

Densities greater than 99% can be reached by a suitable choice of process parameters in L-PBF [57,59]. For high-strength Al alloys with poor processability, it is of great relevance to find the correct process window. An example is given in the work of Stopyra et al. [60], who determined the optimal parameters to manufacture defect-free AA7075 components by L-PBF: they were able to obtain a relative density higher than 99% and low vaporization loss, but it was not possible to completely eliminate solidification cracks.

The quality and properties of feedstock materials, powders in particular, have a crucial relevance on the resulting printed parts. Tests on morphology, size distribution, apparent density, and flowability are usually made on the powders before printing. Deviations from optimal values of these parameters can result in the higher density of defects; therefore, they are strictly correlated to moisture absorption, surface energy, and cohesion potential, and they affect the homogeneity and distribution of the powder layer. Tests on AlSi7Mg powders with different particle sizes showed that fine spherical particles ($\sim 9 \mu\text{m}$) are more susceptible to water absorption and powder cohesion than particles of larger size (40–48 μm) [61–64]. Samples printed by using fine powders show lower density ($\sim 95\%$) than those printed with coarse powders ($\sim 99\%$). Moreover, coarse powders lead to lower top surface roughness, better dimensional accuracy, and greater hardness due to finer cellular structure [63,64].

Moisture on the powder surface must be avoided, not only because it influences the powder distribution but also because it can lead to the formation of hydrogen pores [65,66]. A viable solution can be a drying process to remove water on the powder surface before printing. In Al12Si, drying modifies the powder surface, reducing oxide formation that could give rise to defects in printed parts. Through this treatment, it is possible to obtain final parts with a 99.9% relative density.

Another relevant issue in industrial production by AM technologies is the use of recycled powders. Tonelli et al. [58] observed that spherical powders lead to the manufacturing of components with higher density and less spattering defects than those printed using powders of irregular shape, and such behavior has been explained by considering the better flowability of spherical powders. Generally, recycled powders show an irregular morphology; thus, they are expected to give rise to printed parts of lower quality compared with those obtained using fresh powders. However, Maamoun et al. [59] demonstrated that it is possible to obtain the same density (99.7%) by printing parts with fresh and recycled AlSi10Mg powders if laser power is high enough (370 W). These investigators also observed that such density is comparatively higher than that (95.6 to 99.6%), reported in the literature in processes using fresh powders but performed under lower laser power (100–350 W) [53,54,56,67].

In conclusion, porosity is a multivariable problem, because it depends in many ways on material composition and process parameters, and it is quite difficult to find the optimal trade-off of all these factors. A lot of papers can be found in the literature on the matter (only some of them are cited here); however, the major part is focused on specific aspects. Therefore, it seems important to put more efforts in the future to investigate the process of a single material in a whole by combining experimental work and simulation.

3.2. Hot Cracking

Another issue of serious concern in the production of Al alloys by AM techniques is hot cracking due to metal shrinkage during solidification. It preferentially takes place in alloys with a large temperature range of solidification, owing to the lack of liquid metal in the interdendritic spaces. In different Al alloys, the phenomenon exhibits the following characteristics: (i) cracks are parallel to the building direction [68,69], (ii) notch effect can lead to cracks initiated by pores [70], (iii) cracks could propagate along grain boundaries [70], and (iv) equiaxed semisolid structures partially accommodate the strain and mitigate the cracking [70].

Figure 7, taken from ref. [68], shows how an increasing content of Si in 7075 alloy reduces cracking susceptibility.

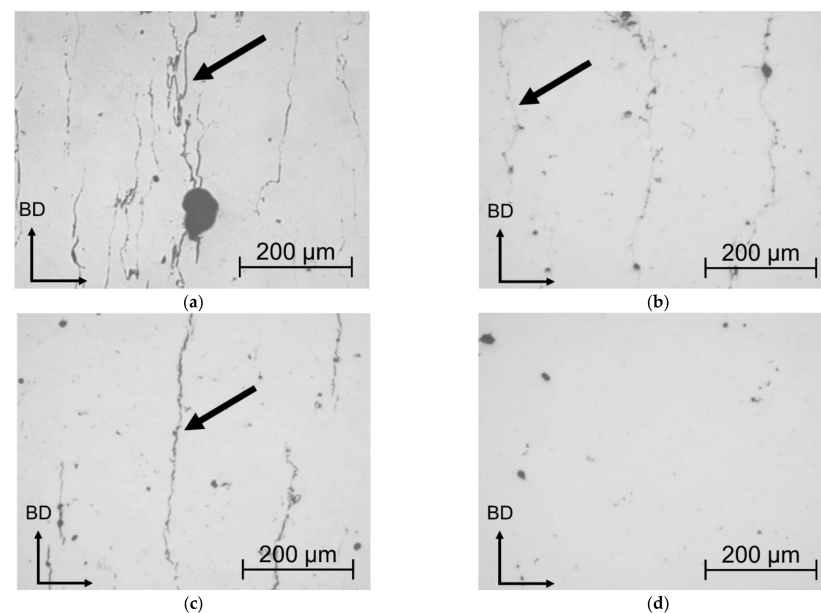


Figure 7. Cross-sections of 7075 alloy without Si (a) and with 1 wt% (b), 2 wt% (c), and 4 wt% (d) of Si. Cracks parallel to the building direction (BD) are indicated by arrows. Adapted from ref. [68] (reproduced with permission from Journal of Materials Processing Technology; published by Elsevier, 2016).

One of the possible solutions is the modification of the alloy composition. For instance, the addition of Sc and Zr has beneficial effects, because it leads to the formation of $Al_3(Sc,Zr)$ precipitates, acting as preferred nucleation sites and promoting a microstructure with fine and equiaxed grains [71–76].

According to Hu et al. [77], who investigated the SLM of Al–Cu alloys, the center of the molten pool is the most susceptible zone for crack initiation. Therefore, the addition of Si in alloy composition reduces hot cracking by increasing the amount of eutectic. Other factors that influence hot cracking are the amount of dissolved gas, wettability of the solid by the liquid, and process parameters [51]. Scan spacing is a parameter that strongly influences the cooling rate, thus the occurrence of hot cracking [57,78]. Hu et al. [77] developed a general method to determine the critical scan speed in SLM that was verified for two different Al–Cu alloys, namely AlCu5MnCdVA and Al–Cu–Mg–Mn. From a literature review [79–83], they observed that scan speed and cracking susceptibility are directly linked: the latter increases as the speed increases. Their model is based on the modified Rosenthal’s equation and Feurer’s criterion [84], which considers both the material properties and process parameters: by applying this model, the critical scan speed above which the cracks can form at the center of the melt pool is obtained. Solidification temperature range is not the only thing that matters for cracking, because the thermophysical properties, in particular thermal expansion, viscosity, thermal conductivity, specific heat, density, and growth coefficient of secondary dendrite arms, also play a relevant role. Moreover, the multiple thermal cycles during SLM favor crack formation, even if the overlapping of the molten pool can eliminate the cracks which initiate during the previous scanning. Therefore, a small scan spacing could be beneficial for crack reduction [77].

3.3. Anisotropy

Epitaxial columnar grains, parallel to the building direction, are one of the typical features of AM metals; this structure is the main reason for anisotropy in mechanical properties [50]. However, columnar grains are not the only factor that influences the anisotropy of mechanical properties, since lack-of-fusion defects, which can act as stress concentration sites [85], are mostly oriented perpendicularly to the building direction. The result is a difference in mechanical properties along the building direction and perpendicular to it (see examples in Table 1).

Table 1. Anisotropy of mechanical properties in some Al alloys. The anisotropy is defined by $\frac{\sigma_z - \sigma_x}{\sigma_x} * 100$; Z is the vertical direction, parallel to the building direction, and X and Y are the horizontal ones.

Material	Condition	Process	Tensile Axis Orientation	Yield Stress Anisotropy (%)	Elongation Anisotropy (%)	Yield Stress (MPa)	Elongation (%)	Ref.
Al12Si	As-built	SLM	Z XY	−1.7	50	274.8 ± 8 270.1 ± 10	2.2 ± 0.3 4.4 ± 0.7	[86]
Al12Si	HT	SLM	Z XY	2.0	20.8	150.3 ± 17 153.4 ± 5	4.2 ± 0.3 5.3 ± 0.7	[86]
AlSi10Mg	As-built	SLM	Z XY	4.0	16.7	240 250	1 1.2	[53]
AlSi10Mg	As-built	SLM	Z XY	-	37.5	- -	3.47 ± 0.6 5.55 ± 0.4	[87]
Al–Si–Mg	As-built	DMLS	Z XY	4.9	33.9	231 ± 3 243 ± 7	4.1 ± 0.2 6.2 ± 0.3	[88]

Rashid et al. [89] observed that samples of AlSi12 manufactured by SLM in different orientations (0°, 45°, and 90°) do not exhibit significant microstructural differences, while the relative density is different; therefore, they concluded that the resulting anisotropy is linked to the relative density and not to microstructural features. The variations of relative density occur due to the different energy density, because the energy is constant, but the area differs depending on the orientation. Therefore, control of this parameter could reduce

the gap between the mechanical properties along perpendicular directions. Analogous results were obtained by Nezhadfar et al. [90] on AlSi10Mg, Scalmalloy, QuesTek Al, AD1, and AlF357, produced by L-PBF: the samples manufactured with an angle of 0° from the building plate present a higher defects density than the perpendicularly manufactured ones. Among these alloys, Scalmalloy and AD1 show the lowest defect anisotropy due to their lower thermal conductivity.

As observed by Chen et al. [91], anisotropy also affects corrosion resistance: in AlSi12 produced by SLM, corrosion resistance in 3.5 wt% NaCl solution is higher in the building direction than in the perpendicular one.

In the WAAM of ER 5183, defects such as porosity and microcracks have been observed in the regions between adjacent layers, because samples with the main axis transversal to the building direction show lower strength and ductility than those with the main axis longitudinal or diagonal to the building direction [92]. Qin et al. [93] observed that transversely deposited (TD) samples of Sc and Zr-modified Al–Mg alloy exhibited a superior fatigue strength (100.5 MPa) compared with that (57 MPa) of the parallelly deposited (PD) ones and attributed the phenomenon to two factors: defects (lack of fusion resulted in a higher stress concentration in the PD samples) and microstructure. Different crack propagation paths led to different columnar grains/equiaxed grains area ratios and some grains of TD samples ($\langle 110 \rangle //$ building direction) contribute to enhance the fatigue resistance because of the exceptional dislocation formation.

3.4. Poor Surface Morphology

Al components produced by AM commonly present great surface roughness. The main parameters that influence surface roughness are laser power, scan speed, and scan spacing. As laser power increases, the average surface roughness and data scattering increase as well, due to instabilities in the melt pool [94] (see Figure 8).

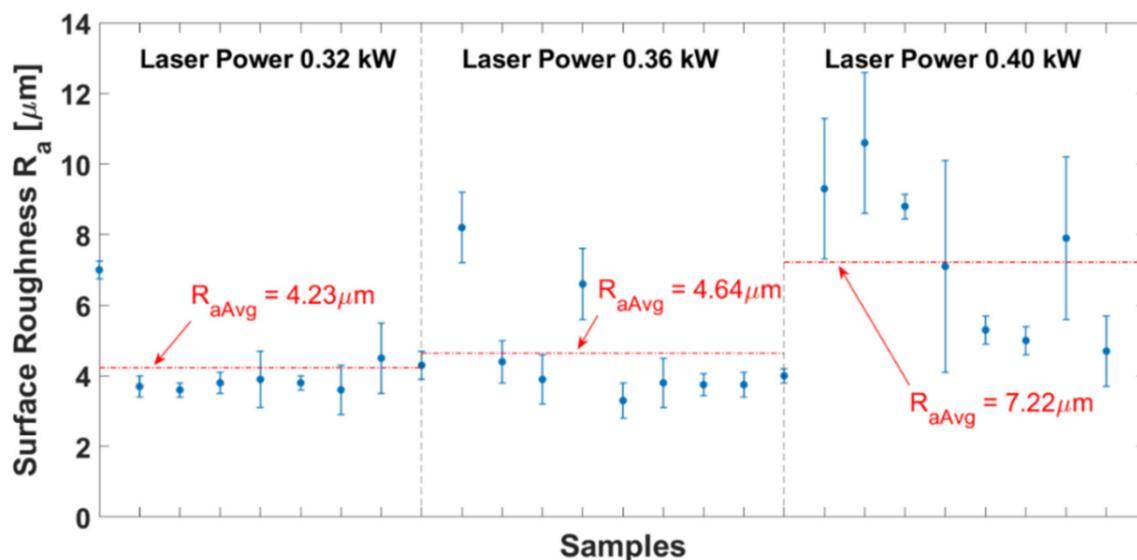


Figure 8. Surface roughness of three groups of samples printed by L-PBF with laser powers equal to 0.32, 0.36, and 0.4 kW (redrawn from ref. [94]).

For a given laser power, lower scan speed leads to lower surface roughness; for example, in Direct Metal Laser Sintering (DMLS) of AlSi10Mg [95], through a suitable tailoring of the scan speed, it is possible to obtain a surface roughness of one fifth of that of samples printed with standard parameters. The phenomenon, also observed in the same material produced by L-PBF [96], is correlated to the melt pool size that depends on both laser power and scan speed.

The overlapping of molten pools in the manufacturing of a single layer depends on hatch spacing: the greater the scan spacing, the lower the overlapping. Generally, great scan spacing leads to poor surface quality in top/bottom surfaces, where it is possible to see the outline of different laser scans, but also on side surfaces.

A model of Majeed et al. [94] provided a relationship to predict surface roughness of AlSi10Mg samples produced by L-PBF given the scan speed (SS), the overlap rate (OR), and the hatch distance (HD), where laser power (LP) is a fixed parameter:

$$R_a(LP) = 6.7 + 10.19 \cdot SS + 0.1709 \cdot OR - 0.552 \cdot HD + 0.00426 \cdot HD^2 \quad (2)$$

Calignano et al. [97] used statistical models to determine the effects of process parameters on surface roughness of AlSi10Mg samples produced by DMLS: the scan speed is the parameter that mostly influences the surface finish followed by scan distance and laser power. In the case investigated by these authors, the optimal parameters are laser power of 120 W, scan speed of 900 mm/s, and scanning distance of 0.10 mm.

3.5. Residual Stresses

Due to the rapid solidification and thermal cycles, printed components often present residual stresses [98,99], which must be avoided, or at least minimized, since they lead to deformation in thin walls and poor fatigue behavior. High tensile stresses in as-built components are often not completely recovered by usual postprocessing operations [100]. In AlSi10Mg produced by SLM, residual stresses vary with the preheating temperature: higher temperature leads to lower residual stresses [101].

Residual stresses induce greater distortions in narrower plates and bars, but preheating can reduce residual stress and consequent distortions regardless of the part geometry [102]. AlSi10Mg printed by SLM exhibits a significant reduction in distortions with preheating at 150 °C, and at 250 °C, distortions become negligible [97].

In Al alloys of 2xxx series produced by WAAM, residual stresses were observed to reach the material yield stress, causing relevant distortions [98]. Hönnige et al. [98] studied the influence of vertical and side rolling on the residual stresses in WAAM samples: vertical interlayer rolling can eliminate the distortions; according to the authors, it also hardens the material, facilitating the natural aging of the alloy. Postprocess side-rolling helps control residual stresses and reduce distortion. According to Oyama et al. [103], in a WAAM of Al5Mg and Al3Si alloys, a viable solution could be to apply an adaptive heat source during the production of components. This reduces the thermal discontinuities during the process and limits the metrological deviations.

4. Microstructure and Mechanical Properties

The microstructure of printed Al alloys exhibits some specific features which strongly affect the mechanical properties of components; among them, hierarchical structure, grain morphology, and precipitates are of particular interest and have drawn the attention of many investigators, together with the effects of printing conditions.

4.1. Hierarchical Structure

The layer-by-layer printing of Al alloys leads to a hierarchical structure [104–108]. Typical microstructural features are melt pools, due to melting and solidification of a small volume of material under the effect of the laser (or other energy source). For example, Figure 9a shows the pattern of laser scans on the surface of an AlSi10Mg sample printed by L-PBF, while in Figure 9b, the semicircular shape of melt pools can be observed on the cross-section of the same sample [109].

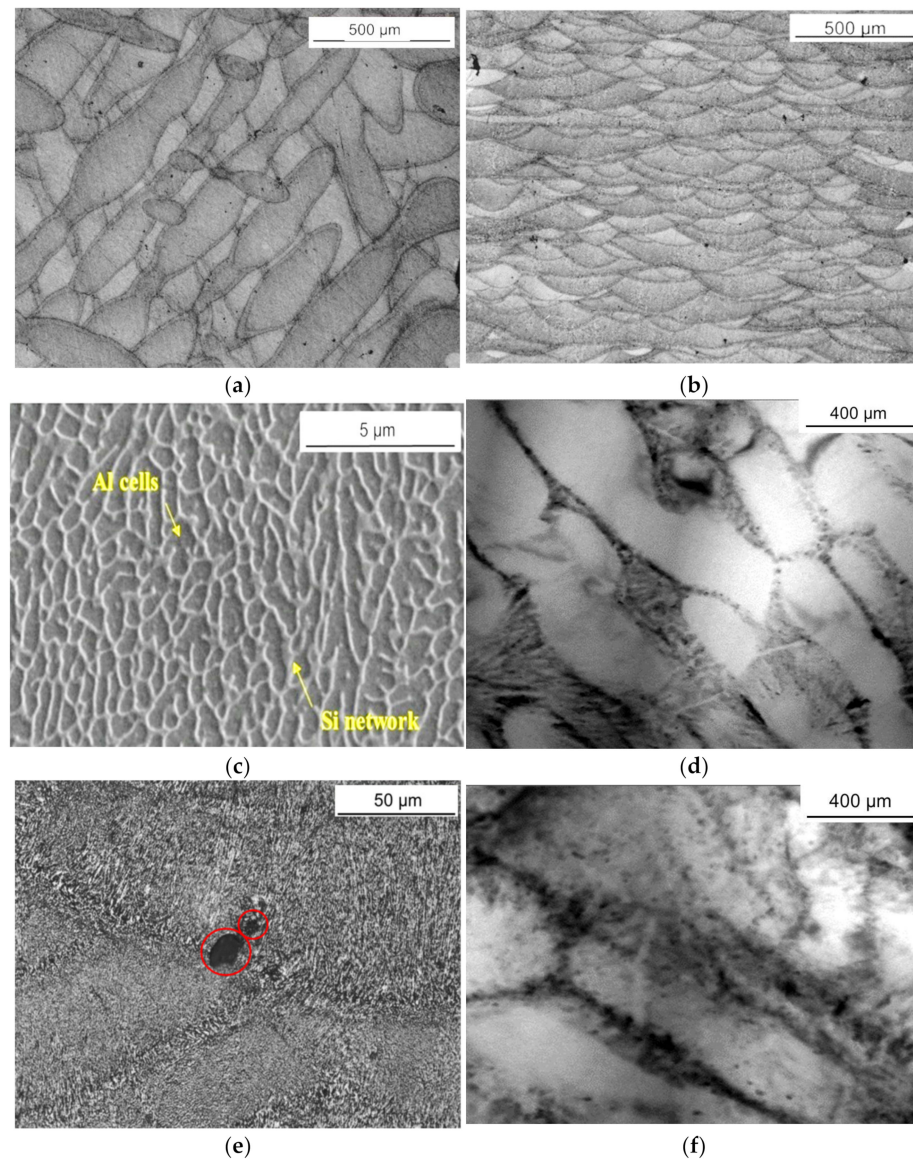


Figure 9. Laser scans on the surface of a AlSi10Mg sample printed by L-PBF (a); melt pools in the cross-section of the same sample (b); each grain inside the melt pool exhibits a finer substructure of cells decorated by eutectic (c,d); pores of micrometric (e) and nanometric (f) size. Micrographs are taken from ref. [109] and other unpublished works of the present authors (b,c,e reproduced with permission from Journal of Alloys and Compounds; published by Elsevier, 2022).

The Al grains inside the melt pools are elongated in the building direction, and each grain exhibits a finer substructure of cells decorated by eutectic (Figure 9c). The average size of the cells is about one order of magnitude lower than that of grains. Moreover, the material exhibits pores with different shapes and sizes (Figure 9e). As also observed by other investigators [110–112], Si atoms are present in the Al matrix above the concentration of equilibrium, and networks of entangled dislocations form in Al as the result of fast solidification ($\sim 10^7$ °C/s), typical of the L-PBF process. The cells and grains present a consistent size, morphology, and texture from top to bottom of the printed parts [113]. The cyclic reheating of the material enhances diffusion, giving rise to the precipitation of different compounds depending on the specific composition of the alloy. As a matter of fact, this phenomenon is an intrinsic heat treatment due to the repeated thermal cycles. In addition, the high Mg susceptibility to evaporation leads to a lack of this element from some parts of the final component, with effects on the properties of the material.

Fite et al. [114] observed that the microstructural features undergo some changes at room temperature in the first hours after the build; in particular, the concentration of Si in the Al matrix decreases, nanoprecipitates nucleate at the center of cells, and preexisting precipitates tend to coarsen. Generally, process parameters strongly affect the microstructures [115], and their effects are discussed in this section.

4.2. Grain Morphology and Precipitation Strengthening

An important microstructural phenomenon occurring during solidification is columnar to equiaxed transition (CET), namely a change in grain morphology [116,117]. During solidification, a high G/R ratio (G thermal gradient, R growth rate) gives rise to the formation of an epitaxial columnar grain zone, while low G/R values promote equiaxed grains. AM technologies may exhibit significant difference in the solidification conditions; for instance, G is 10^5 – 10^6 °C/m in SLM and 10^4 – 10^5 °C/m in WAAM, R is ~ 1 m/s in SLM and $\sim 10^{-3}$ m/s in WAAM, and cooling rate is $\sim 10^7$ °C/s in SLM and 10 – 10^2 °C/s in WAAM. Such differences in solidification conditions involve different G/R ratios and CET. Anyway, in a major part of printed Al alloys, a columnar grain structure develops along the building direction; thus, they exhibit anisotropy of mechanical properties.

Several studies focused their attention on the possibility to promote CET and texture modification in AM components through different strategies, such as the addition of inoculants [23,68,118], change in process parameters in SLM and Electron Beam Melting (EBM) [66,119], various build strategies, laser energy density, and alloy modification.

The presence of elements such as Sc, Zr, Ti, Ta, Ni, and Nb facilitates the formation of equiaxed grains, because their precipitates Al_3X ($X = Sc, Zr, Ti, Ta, Ni, \text{ and } Nb$) act as preferred sites for heterogeneous nucleation due to their very low lattice mismatch with the Al matrix [120]. For example, as shown in Figure 10, the addition of Nb particles (3%) to 7075 alloy processed by L-PBF leads to a complete CET, passing from columnar grains (~ 10 μm width, 100 μm length) to ultrafine equiaxed grains ($d < 3.5$ μm).

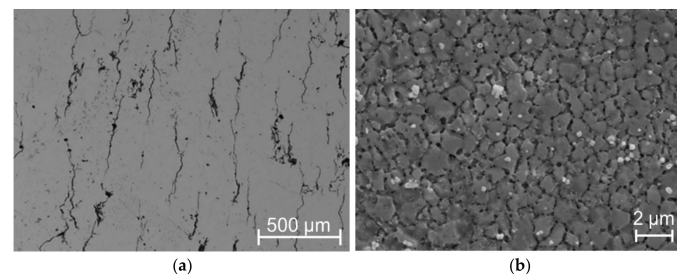


Figure 10. The 7075 alloy processed by L-PBF exhibits a columnar structure (a). After the addition of Nb particles (3%), the structure consists of ultrafine equiaxed grains (b). Adapted from ref. [120] (reproduced with permission from Additive Manufacturing; published by Elsevier, 2022).

Li et al. [121] reported that an equiaxed microstructure with random texture was obtained by adding nanoparticles of TiB_2 to AlSi10Mg during SLM. A similar approach was adopted by Yang et al. [118] with the addition of Sc to the Al–Mg–Zr alloy; in this case, the Al_3Sc particles play a fundamental role in heterogeneous nucleation in the melt pools, and a fully equiaxed microstructure was achieved. Moreover, Al–Mg–Sc–Zr alloys are hardened by aging, so the microstructure can be suitably tailored to have a high fraction of finely dispersed coherent $Al_3(Sc_xZr_{1-x})$ intermetallics for improving mechanical properties [122]. According to these authors, the fast solidification leads to a high quantity of Sc and Zr trapped in the Al matrix; thus, subsequent heat treatments and HIP induce the precipitation of Al_3Sc particles by a factor of ~ 3 – 10 times compared with the as-built condition.

In general, in AM technologies, there is a narrow window of process parameters to achieve CET. Hadadzadeh et al. [123] found that the grains of AlSi10Mg printed by DMLS switch from columnar to equiaxed by changing the building direction from vertical to horizontal: 75% of columnar grains in vertical samples and 49% in horizontal samples.

CET alters the shape and consistency of Si precipitates and dislocation density in the α -Al dendrites: in the vertical samples, they found a fine coherent dispersion of Si precipitates, while in the horizontal samples, Si precipitates are bigger and noncoherent, and the dislocation concentration is smaller. According to these investigators, the transition depends on the angle between the nominal growth rate and the $\langle hkl \rangle$ direction of the dendrite.

Today, aircraft components of large size, such as wing ribs and fuselages, are still manufactured through conventional techniques, namely milling and forging. A lot of work is still focused on these processes to obtain the optimal precipitate distribution, reduce the microstructural heterogeneity by grain refining, and improve the mechanical properties, and in particular, enhance the fracture toughness without detrimental effects on yield stress and ultimate tensile strength (e.g., see refs. [124–127]). However, WAAM technology has attracted increasing interest for producing near-net structures with reduced costs and high efficiency. Significant progress has been made by investigating the application of WAAM to different Al alloys, including Al–Cu, Al–Mg, Al–Si, Al–Cu–Mg, and Al–Mg–Si [128–135]. Alloys for structural aeronautic applications must guarantee relevant mechanical properties; thus, WAAM has been used to produce more complex materials such as Al–Zn–Mg–Cu alloys. Since their first application in the Japanese Zero fighter aircraft, these alloys have been of great interest for the aeronautic industry, owing to their high specific strength, excellent toughness, and fatigue resistance, achieved by aging treatments inducing a fine and homogeneous distribution of the η phase.

Dong et al. [136] investigated the 7055 alloy produced by WAAM and evidenced that in a single-layer deposition, there are two types of columnar grains (one originated from the starting position and the other one from the bottom fusion lines), with different orientations. As shown in Figure 11, the grains originated from the starting position are partially remelted during the deposition of the subsequent layer, giving rise to a periodical microstructure.

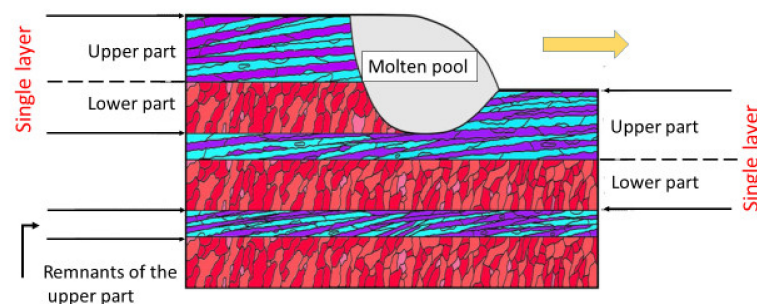


Figure 11. Mechanism of formation of the two types of columnar grains during WAAM of 7055. Redrawn from ref. [136] (reproduced with permission from Additive Manufacturing; published by Elsevier, 2020).

Another interesting characteristic is the presence of second phases with both micrometric ($\text{Mg}(\text{Zn,Cu,Al})_2$ and $\text{Al}_7\text{Cu}_2\text{Fe}$) and nanometric ($\text{T}(\text{Al}_2\text{Mg}_3\text{Zn}_3)$ and $\eta(\text{Mg}(\text{Zn,Cu,Al})_2)$) size.

Zhou et al. [137] produced a 2219 alloy by WAAM with a heterogeneous band structure consisting of an alternating distribution of equiaxed and columnar grains. The volume fractions of equiaxed and columnar grains were varied by adjusting the cooling mode of the substrate.

Other alloys of the Al–Cu family of interest for aeronautic applications are those containing Mg and Ag, because Ag enhances precipitation strengthening by promoting the formation of the Ω phase [138,139]. The A201 alloy, developed about 60 years ago, showed relevant strength but poor castability. Generally, these alloys exhibit high susceptibility to hot tear formation; therefore, a new generation has recently been developed to overcome these limitations.

In the development of high-strength Al alloys tailored specifically to AM, L_{12} - Al_3X -forming elements are particularly effective to (i) reduce the susceptibility to solidification

cracking by grain refinement and (ii) increase the strength by forming secondary nanoscale precipitates. A significant example is reported by Roscher et al. [140] regarding Al1.76Ti and Al2.51Ti (wt%) alloys manufactured by L-PBF.

One of the most investigated alloys of this novel generation is the A205 alloy (Al–Cu–Mg–Ag–Ti–B), owing to its fine microstructure, excellent strength and toughness over a broad range of working temperatures, and good compatibility with both conventional and AM technologies [141]. These characteristics are achieved by adding Ti (3.00–3.85 wt.%) and B (1.25–1.55 wt.%) in the form of TiB₂, which promotes the formation of intermetallics. With respect to Sc and Zr, which also refine the grains through the formation of Al₃Sc and Al₃Zr nucleants at temperatures in the range 1500–2000 °C [73], TiB₂ keeps its stability up to 3500 °C [142]. As elucidated by Carluccio et al. [143], the presence of TiB₂ restricts grain growth even at the high temperatures involved in the laser melting process. These investigators found that, when Sc is added to AA6061 and Al7Si alloys, a mix of fine equiaxed and fine-to-moderated size columnar grains unevenly nucleate and grow within the melt pools during SLM; the same materials microstructurally modified by TiB₂ show a homogeneous distribution of fine equiaxed grains over the entire melt pools without preferential crystallographic orientations [144]. This fine grain structure is resistant to the intergranular cracking and shrinkage porosities observed in A201 and other Al–Cu alloys with coarse columnar morphology.

4.3. Printing Conditions

The mechanical properties depend on the specific AM process and process parameters used to build the part. Printed metallic alloys often exhibit improved strength and hardness if compared with the same as-cast and wrought materials due to the finer microstructure (e.g., see refs. [113,145]), while the presence of unmelted powder and pores, they can decrease the ductility and Young's modulus, which is strongly affected by porosity. This has been confirmed by Mechanical Spectroscopy (MS) investigations carried out on AlSi10Mg produced by both casting and L-PBF [110,146]. More details about the technique that can be used to investigate various phenomena of metals can be found in refs. [147–151].

As shown in Figure 12, in the first test run, the dynamic modulus of AM alloy exhibits an anomalous trend: as temperature increases, the modulus is expected to monotonically decrease, owing to anharmonicity effect; however at ~170 °C, it starts to increase, exhibits a maximum at ~210 °C, then decreases again. After cooling at room temperature, the modulus is increased by about 7%, while the density passes from 2.39 g/cm³ (as-built material) to 2.52 g/cm³. The modulus is not further modified by successive test runs. SEM and TEM observations allowed to explain the phenomenon, which does not occur in the same as-cast alloy, as the closure of pores of nanometric size.

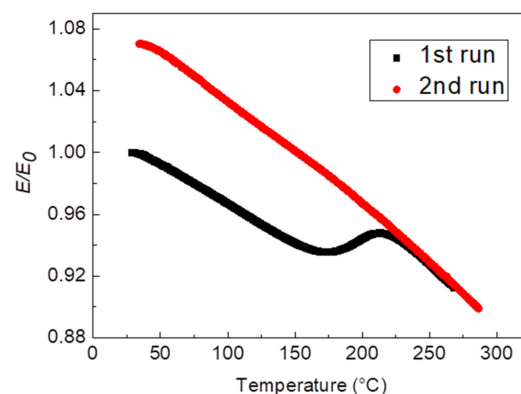


Figure 12. Dynamic modulus E vs. temperature of the AlSi10Mg alloy manufactured by L-PBF measured in two successive test runs. The values of dynamic modulus are normalized to the value E_0 measured at room temperature in the 1st test run. Redrawn from ref. [109] (reproduced with permission from Journal of Alloys and Compounds; published by Elsevier, 2022).

Another aspect relevant to industrial AM processes is the use of recycled powders. The analysis of the microstructure of AlSi10Mg samples printed from virgin and recycled powders shows differences in terms of Si precipitate characteristics, cell size, and dislocation density. According to Hadadzadeh et al. [152], recycled powders contribute to strengthen the alloy through the Orowan mechanism (more Si precipitates), Hall–Petch effect (formation of eutectic cell walls), and dislocation hardening. A possible drawback of the use of recycled powders is their higher content of inclusions, which form because of the great reactivity of Al with O [41].

Maamoun et al. [59] demonstrated that the use of recycled powders is not an obstacle to achieving the optimal mechanical properties of AlSi10Mg printed by SLM, if suitable postprocess heat treatments are adopted.

AM processes carried out in noncontrolled environment (e.g., SLM) or with nonoptimal shielding gas flow rate (WAAM) may lead to the formation of oxides which then remain trapped in the metal during solidification; thus, the right choice of process parameters can have a great impact on the oxidation and the resulting inclusions [56]. SEM observations on the fracture surfaces of 6061 samples evidenced that thin oxides films are present in the material, especially in the sides of the melting tracks, with a related decrease in ductility. The model of Louvis et al. [46], presented in the previous section, well describes the phenomenon.

Different approaches have been proposed to refine the microstructure and obtain high density parts.

Mohammadpour et al. [153] showed how Solidification Microstructure Selection (SMS) maps, obtained from solidification models, can help to predict the microstructure based on the solidification parameters. A very important parameter is the energy density of the beam used to melt the metal; higher energy densities, which are helpful to limit the defects in the built components, also promote microstructure coarsening and consequently lower mechanical properties of the printed parts [96].

Various works highlight the influence of shielding gases used during the process [154]: the preheating temperature of the building plate and chamber [155] and the orientation of the part in the printing space [156].

The shielding gases used in AM usually are inert gases, such as Ar. Li et al. [154] used N₂ as shielding gas to print 5356 Al samples by using the WAAM technique. Comparing the results with those obtained with Ar, they observed smaller grains, hardness increase of ~12%, and ductility reduction due to the presence of a large number of nitrides formed during the printing process.

Bian et al. [155] obtained a ~100% dense AlSi10Mg alloy by EBM with good surface finish and refined microstructure, consisting of a bimodal microstructure of coarse grains and fine subgrains. They achieved such excellent results through a suitable choice of preheating temperature and scan speed. Preheating the building platform (300 °C) allows to produce AlSi10Mg by SLM with a more homogeneous microstructure with globular Si particles and no apparent differences in samples with different printing direction (0°, 45°, and 90°). The effects of preheating on microstructure and mechanical properties of A357 manufactured by L-PBF were also studied by Aversa et al. [156]. They proved that preheating at 140 °C and 170 °C promotes an in situ ageing treatment, leading to a ~17% higher ultimate tensile strength, values comparable to those of the same alloy produced by casting and T6 treated.

AlSi10Mg samples produced by SLM show a fatigue resistance dependent on growth direction; in particular, those grown at 0° (growth angle) present a higher fatigue resistance. The same alloy produced with heating of the build platform (300 °C) exhibits a better fatigue behavior and negligible differences in the three examined building directions (0°, 45°, and 90°) [157,158].

5. Tailoring of Alloy Composition

The Al alloys most used in AM processes are the near eutectic Al–Si ones such as Al12Si, A357, A356, and AlSi10Mg, because their solidification range is much narrower

with respect to other high-strength alloys such as 2024. Moreover, Si improves the fluidity of liquid Al and favors laser absorption in the L-PBF process. One of the main problems related to the 3D printing of Al is its low absorptivity, and the presence of Si and Mg as alloying elements improves the absorptivity and consolidation kinetics [159]. Alloys with Si and Mg have higher packing density, and there is a reduction in input heat. Moreover, Si partly prevents Al oxidation and reduces the thickness of the oxide layer. In general, Si and Mg broaden the processing window.

Apart from AlSi10Mg, the high-strength Al alloys such as those of 2xxx, 6xxx, and 7xxx series can hardly be manufactured by L-PBF because of their hot cracking susceptibility during solidification and the high volatility of alloying elements such as Zn, Mg, and Li, which easily evaporate during the process [160]. The risk of failure to create dense samples from age-hardenable Al alloys is very high, even if densities above 99% have been achieved by manufacturing AW-2022 and AW-2024 under variations of laser power, scan speed, and scan spacing [161].

High-strength alloys were originally designed for conventional manufacturing processes, while L-PBF provides higher cooling rates (up to 10^7 °C/s); thus, elements can be quenched into solid solution in concentrations far above the maximum equilibrium solubility. Therefore, rapid solidification extends the range of elements that can be applied for precipitation hardening.

Moreover, Al–Fe–V–Si series heat-resistant Al alloys have received considerable attention due to their low density, excellent thermal stability, high specific strength, and high specific stiffness. These alloys have the potential to replace some of the Ti alloys applied in aviation industries at temperatures up to 400 °C. Full dense AA8009 (Al–8.5Fe–1.3V–1.7–Si by wt%) alloy parts were fabricated by SLM with a few build defects and chemical composition similar to that of precursor powders, despite a slight Al loss and a low O pickup [162].

Tailoring alloy composition can have beneficial effects on the choice of process parameters and the final properties of components. Alloying elements can improve absorption, allowing a reduction in laser power; influence the thermal expansion and solidification range of the alloy; form stable precipitates; and act as grain refiners.

Among the alloying elements added to Al alloys to improve their performances, Sc plays a dominant role. Soviet metallurgists developed the first Sc-containing Al alloys, which were implemented on the MiG-21 and MiG-29 aircrafts. Minor additions of Sc (<0.5%) remarkably increase the strength of Al alloys (>30%) because of Al₃Sc precipitates homogeneously dispersed into the Al matrix. Some decades later, engineers at Airbus came up with a second-generation alloy (Scalmalloy), also containing Zr, whose composition is reported in Table 2.

Table 2. Chemical composition of Scalmalloy.

Element	Mg	Sc	Zr	Mn	Si	Fe	Zn	Cu	Ti	O	V
wt %	(min)	4.00	0.60	0.20	0.30	0.00	0.00	0.00	0.00	0.00	0.00
	(max)	4.90	0.80	0.50	0.80	0.40	0.40	0.25	0.10	0.15	0.05

Scalmalloy exhibits an excellent strength-to-weight ratio; thus, it is an ideal material for use with TO tools in the aeronautic industry. This alloy offers benefits few AM metals can boast by combining the lightness of Al with almost the same specific strength and ductility of Ti6Al4V [71,163]. In addition, compared with other Al alloys for AM, Scalmalloy has a unique level of corrosion resistance and a stable microstructure at elevated temperature.

Zhang et al. [164] successfully fabricated a high-performance Al–Mg–Sc–Zr alloy by SLM and investigated the thermodynamics of precipitation and its influence on mechanical properties. Recently, Agrawal et al. [165] designed a novel alloy (Al1.5Cu0.8Sc0.4Zr), showing a good combination of strength and ductility in both as-built and aged conditions with a defect volume of about 1%. The aged samples show higher mechanical properties

due to coherent precipitates and the presence of Cu-rich regions. Since in as-built conditions columnar grains act as preferred crack nucleation sites, the precipitation of new phases at grain boundaries during aging allows to overcome this drawback.

A lot of conventional Al alloys of the 2xxx, 6xxx, and 7xxx series, commonly used for structural applications in aircraft, have been manufactured by means of AM technologies; however, they suffer from hot-tearing. For a wider diffusion of beam-based AM in the aeronautic industry, the design and development of high-strength Al alloys with good L-PBF processability is considered as one of the main challenges. Therefore, the addition of grain refiners [71,122,166–171] and modification of alloy composition [172,173] have been used to overcome, or at least reduce, this disadvantage.

The addition of Sc and Zr has also been used by Qi et al. [174] to develop a new Al–Li alloy (Al–Cu–Li–Sc–Zr) to be processed through L-PBF. This alloy was successfully printed with a high building rate and low loss of Li, obtaining a mix of fine equiaxed and columnar grains and good mechanical properties due to grain refinement (yield strength = 482 ± 1 MPa; ultimate tensile stress = 539 ± 1 MPa; and elongation = $8.8 \pm 0.7\%$).

To reduce hot cracking, the combination of Zr and Cu has also been studied [175]: Cu promotes the segregation of an eutectic Al–AlCu phase during the final stages of solidification [176–178], while Zr refines the microstructure and favors the formation of equiaxed grains [179]. A Sc/Zr-modified Al–Mg alloy was prepared by both SLM and DED, and due to the different precipitation behaviors of the primary $\text{Al}_3(\text{Sc,Zr})\text{-L}_{12}$ nucleation sites, a heterogeneous grain structure (ultrafine equiaxed grains bands and columnar grains domains) was formed in SLM samples, while a fully equiaxed grain structure was obtained in samples manufactured by DED [180]. As-built SLM samples exhibit the best combination of strength and ductility.

Zhang et al. [181] found that the introduction of Ti into the Al–Cu–Mg alloy effectively promotes grain refinement and CET because of the heterogeneous nucleation provided by Al_3Ti precipitates. Hot tearing cracks were eliminated after Ti modification due to the formation of a homogeneous and fine equiaxed microstructure. The novel high-strength Al–Cu–Mg–Ti alloy exhibits improved tensile strength, yield strength, and ductility.

As shown in Figure 10, 3 wt. % of Nb added to 7075 alloy processed by L-PBF modifies the grain structure from large columnar grains into ultrafine equiaxed grains and completely suppresses hot tearing [120].

Among Al alloys, those containing Li are of particular interest for aeronautic applications, because this element strongly increases the specific mechanical properties (e.g., see refs. [4,182,183]). However, it is well known that optimal mechanical properties of ternary Al–Cu–Li alloys can be achieved by the strict control of the Cu/Li ratio, because it influences the precipitation sequence [183]: a high Li content favors the precipitation of the metastable δ' phase that is undesired, because it is prone to shear localization with consequent poor toughness and ductility. The optimal composition was found to be ~3 wt. % Cu and <1.5 wt. % Li. By using an ultrashort pulse laser, Yürekli et al. [184] exploited the very fast cooling rate to print Al–Li alloys with high Li content (4 wt. %) and with an extremely low amount of δ' phase. In their experiments, these investigators printed parts of relatively low density (~75%); however, Li et al. [185] demonstrated that is possible to reach an acceptable relative density by controlling the process parameters, in particular the scan speed. In general, for Al–Li alloys, AM exhibits clear advantages with respect to conventional manufacturing methods, which are limited by the high chemical activity of Li.

A system of particular interest for high-temperature applications is the Al–Ce eutectic alloy [186–196], which is suitable for AM process due to its narrow solidification range. An example taken from the paper of Bahl et al. [186] is displayed in Figure 13a, comparing the Scheil curve of the $\text{Al}_{7.78}\text{Cu}_{4.73}\text{Ce}$ alloy with that of the AlSi10Mg , AA2024, and AA7075 alloys. The hot-tearing susceptibility index C , calculated by these investigators and reported in Figure 13b, is clearly much lower for the alloy containing Ce.

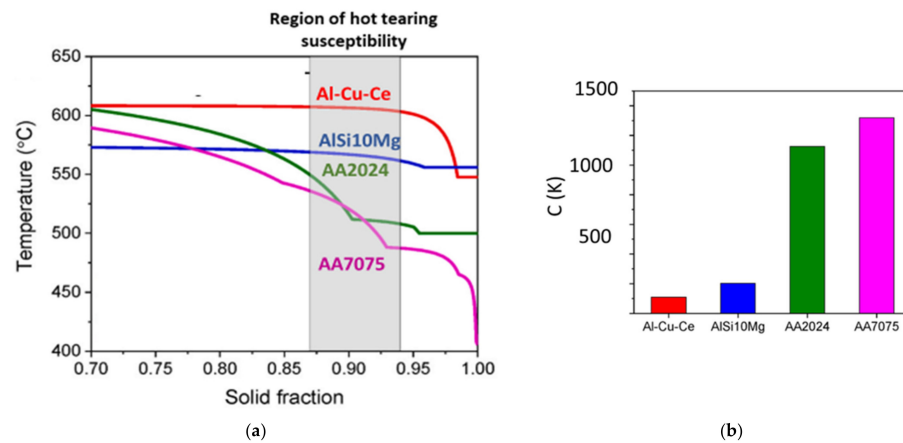


Figure 13. (a) Comparison of Scheil curves (at high solid fractions) of Al–Cu–Ce, AlSi10Mg, AA2024, and AA7075 alloys. The shaded region in (a) marks the range of solid fraction over which the hot-tearing susceptibility index C reported in (b) is calculated. Redrawn from ref. [186] (reproduced with permission from Additive Manufacturing; published by Elsevier, 2021).

The strength at high temperature of the Al–Cu–Ce alloys depends on the spacing (~ 300 nm) and thermal stability of the intermetallics ($\text{Al}_8\text{Cu}_3\text{Ce}$) in the eutectic structure. The spacing between intermetallic particles in the eutectic alloys is inversely proportional to solid–liquid interface velocity, which in turn increases with laser scanning speed during AM [197]. Therefore, alloys with increased strength can be potentially produced by adopting higher laser scanning speed. The particle spacing can also be refined by changing the alloy composition to increase particle volume fraction, and a further contribution could be achieved by additional elements altering the eutectic solidification [195].

According to the criteria suggested by Knipling et al. [198], since the particle thermal stability is related to the slow diffusivity of Zr in the Al matrix, the addition of further elements such as Ti, V, and Cr, with even slower diffusivity, can increase thermal stability. By exploiting the same strategy of grain refinement and precipitation strengthening, other metallic systems have been investigated. For instance, a nearly full dense high-strength AlNd8Ni5Co2 alloy [199] has been produced by SLM, and the material has a composite microstructure with intermetallic AlNdNi₄, Al₄CoNi₂, and AlNd₃ platelets dispersed in the Al matrix.

Through SLM, Al–Ni–Ti–Zr components have also been printed with strategies involving grain refinement through heterogeneous nucleation and eutectic solidification. These parts exhibit a lack of hot cracking in a wide parameter window [200].

Aversa et al. [201] improved the mechanical properties of the AlSi10Mg alloy with the addition of Cu and Ag.

Belelli et al. [202] modified the composition of the 2618 Al alloy by adding low amounts of Ti (2.3 wt. %) and B (0.8 wt. %), and the samples processed by L-PBF exhibited a relative density higher than 99.7%. Ti and B form Ti₂B particles acting as preferred nucleation centers for grains of primary α -Al; thus, microstructure consists of equiaxed grains with excellent resistance to hot cracking.

6. Postprocess Treatments

Postprocess treatments are mainly carried out to induce an optimal distribution of precipitates, reduce porosity and inclusions, improve surface quality, and relieve residual stresses.

6.1. Aging Treatments

In many Al alloys prepared by AM, the rapid solidification leads to a supersaturated solid solution; therefore, aging treatments are usually performed to induce precipitation and strengthen the material [177,203]. Problems involved in aging treatments are those typical of Al alloys; in particular, it is important to find the suitable temperature–time

combination to obtain a fine dispersion of precipitates for optimizing mechanical properties. In addition, treatments should not produce coarsening of the fine microstructure induced by AM processes. To predict the microstructure evolution, which is rather complex and plays a critical role in determining mechanical performances, some numerical models have been proposed (e.g., see ref. [204]).

According to Fite et al. [114], holding AlSi10Mg at room temperature and a subsequent 170 °C aging leads to the formation of Si precipitates at the center of Al cells, as well as the preservation of eutectic ribbons. In this way, they achieved a hardness that is 47% higher than that obtained through conventional solution treatment and 170 °C aging.

The effect of low-temperature annealing at 225 °C on creep behavior was investigated by Paoletti et al. [205] in experiments carried out at 150, 175, and 225 °C. The comparison with data of as-printed alloy demonstrated that annealing results in a loss of creep resistance that is more pronounced at lower temperatures. In general, the creep response of as-printed and annealed alloy becomes more and more similar as temperature increases. The creep behavior was compared with the prediction of a physically based model, considering the effect of Si particle ripening. In such a model, the complex microstructure of the AM AlSi10Mg manufactured by SLM was assimilated to that of a composite formed by soft zones (cell interiors) and hard zones (Si-rich eutectic regions). The constitutive equations were then used on the resulting simplified material model described by the rule of mixture. On the basis of the excellent agreement between data from experiments and the model, they concluded that the key factors determining the creep response are the size and distribution of the second-phase particles: annealing causes an increase in particle size with consequent decrease in creep resistance.

For AlCu5MnCdVA manufactured by SLM, conventional aging methods cannot be implemented due to the loss of Cd during manufacturing. Hu et al. [206] systematically studied different aging treatments to determine the optimal temperature–time combination and avoid θ' coalescence with detrimental effects on mechanical properties. The dominant strengthening mechanism is the fine dispersion of θ' (with high aspect ratio) and θ'' precipitates. Their results are summarized in Table 3.

Table 3. Effect of different heat treatments on AM205A alloy: geometrically necessary dislocations (GND), type of precipitate phases, their volume fraction, yield stress (YS), and ultimate tensile strength (UTS). Data taken from ref. [206].

Treatment	GND Density (m^{-3})	Main Precipitates	Volume Fraction (%)	YS (MPa)	UTS (MPa)
As-built	7.2×10^{13}			155.5 ± 1.5	317.3 ± 1.2
Solution + Natural Aging	3.3×10^{13}	θ'' θ'		217.2 ± 20.4	412.7 ± 15.6
Solution + Artificial Aging (426 K, 10 h)	5.5×10^{13}	θ'' θ'		282.1 ± 15.1	458.0 ± 10.7
Solution + Artificial Aging (426 K, 24 h)	4.8×10^{13}	θ'' θ'	3.67 0.53	345.4 ± 15.5	470.6 ± 6.5
Solution + Artificial Aging (426 K, 48 h)	4.3×10^{13}	θ'' θ'	4.29 1.49	383.3 ± 10.8	476.2 ± 6.4
Solution + Artificial Aging (446 K, 2 h)	4.4×10^{13}	θ'' θ'	1.51 0.10	262.8 ± 5.7	437.3 ± 22.1
Solution + Artificial Aging (446 K, 6 h)	3.7×10^{13}	Mixed θ''/θ'	3.27	352.5 ± 10.5	453.3 ± 5.0
Solution + Artificial Aging (446 K, 10 h)	4.1×10^{13}	Mixed θ''/θ'	3.35	344.7 ± 14.4	441.5 ± 8.7

An interesting phenomenon, namely a multiple precipitation pathway, was observed by Rao et al. [207] in A357 samples manufactured by SLM. Si particles with random crystallographic orientations are the dominant precipitates at the direct aged condition, whereas the precipitation sequence resembles that of cast Al–Si–Mg alloys with solid

solution treatments of 1 or 8 h. However, the main precipitates at peak-aged condition are premature B' (1 h) and β'' (8 h), respectively. Uniaxial strains in the Al matrix seem to be responsible for such unusual precipitation pathways, because they reduce the vacancy formation energy, and both the diffusivity of solutes and nucleation of some precipitates (randomly oriented Si particle and B') are enhanced by the increased vacancy concentration.

6.2. Reduction in Porosity and Improvement of Surface Quality

Since pores, inclusions, and poor surface finish represent preferential sites for fatigue crack initiation, different postprocess treatments have been studied for improving fatigue resistance of printed components, in particular, surface polishing, Shot Peening (SP), and Hot Isostatic Pressing (HIP) (e.g., see ref. [208]).

In some cases, surface polishing after fabrication may present relevant drawbacks, such as unacceptable costs and impossibility to perform the treatment because the surface is inaccessible. Moreover, as evidenced by Nicoletto [209] investigating AlSi10Mg prepared by L-PBF, fatigue behavior is sensitive to the applied stress direction with respect to build direction.

In AlSi10Mg, it has been shown that SP causes shrinkage and collapse of pores, reducing the overall porosity by 0.1–0.3%, and it is more effective in a layer of about 500 μm near the surface [56]. This leads to greater fatigue resistance in both low- and high-cycle fatigue tests [55]. By comparing different surface treatments, Uzan et al. [210], whose results are displayed in Figure 14, showed that the optimal fatigue behavior of the AlSi10Mg alloy produced by SLM can be obtained after surface polishing and SP treatment.

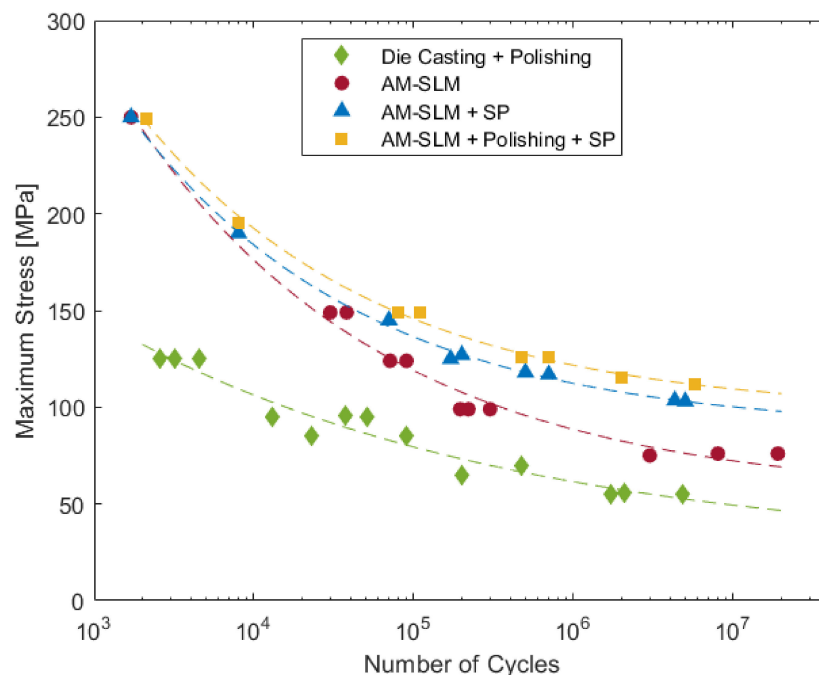


Figure 14. S–N curves of die cast and SLM AlSi10Mg samples in different conditions, namely as-printed, after polishing, and after polishing plus shot peening (SP). Redrawn from ref. [210] (reproduced with permission from Additive Manufacturing; published by Elsevier, 2018).

HIP is an effective solution to reduce porosity of printed materials [211,212], however the microstructural evolution due to soaking at high temperature must be carefully taken into account. For instance, a reduction in the fatigue resistance of AlSi10Mg probes submitted to SP and HIP at 500 °C, with respect to the as-built alloy has been reported and attributed to the coarsening of Si particles [211].

The combination of HIP and standard heat treatments can be performed on printed Al alloys with promising results. For example, T6 treatment after HIP leads to a homo-

geneous distribution of Si particles in Al matrix without significant grain growth due to particle pinning of grain boundaries; the final result is an improvement of mechanical properties [212]. On the contrary, the same treatment performed on the alloy that did not undergo previous HIP results in a reduction in hardness [55]. The explanation of the different effect of T6 treatment is related to unsolvable gases present inside the printing chamber which remain trapped in the pores. T6 treatment, performed at high temperature, promotes gas expansion in the pores and material flow; this does not occur if as-built material is previously submitted to HIP that closes the pores [213].

A different solution is to perform HIP and heat treatment in a single step (Giovagnoli et al. [213]). Finally, another approach involves variations of standard heat treatments; for instance, Di Egidio et al. [214] performed a rapid solution (10 min at 510 °C) followed by artificial aging (6 h at 160 °C). The rapid solution prevents pore growth, leads to a more homogeneous distribution of Si particles in the Al matrix, and limits diffusion of Si and Mg, so these elements remain trapped in solid solution and can form precipitates during the following aging treatment.

To neutralize differences in fatigue life for the 0°, 45°, and 90° directions, Brandl et al. [158] successfully investigated the possibility to combine platform heating (300 °C) and peak-hardening treatment.

6.3. Relieve of Residual Stresses

Thermal cycles during AM process cause residual stresses in printed components, which tend to induce crack extension and structural deformation affecting their quality and performance.

Salmi et al. [100] investigated the effect of stress relief treatments and SP on AlSi10Mg prepared by SLM. They found out that residual stresses, measured by hole drilling method, are tensile stresses and have an oscillatory nature (see Figure 15). Such residual stresses are reduced but not completely eliminated by heat treatments (300 °C for 3 h) while successive SP induces a more uniform stress state and, most important, a compression state near the surface (good for fatigue behaviour).

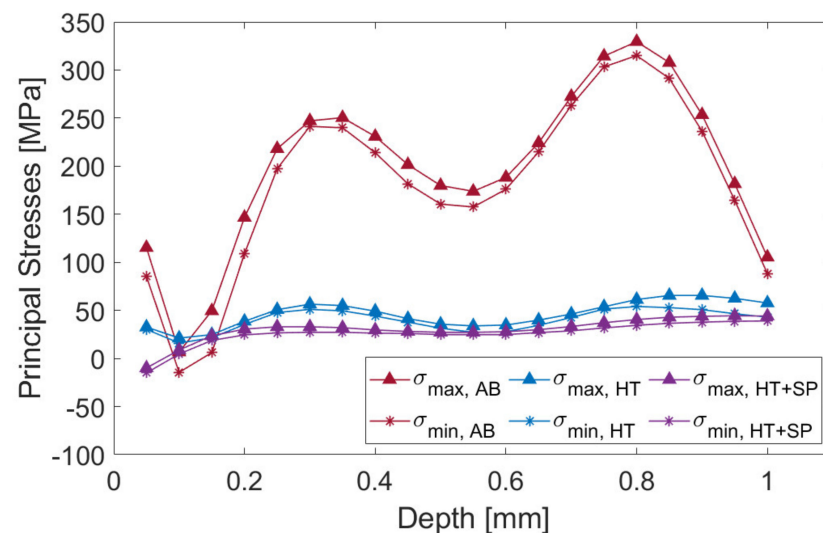


Figure 15. Values of residual stresses vs. distance from top surface of AlSi10Mg samples: as-built (AB), after heat treatments (HT) at 300 °C for 3 h, and after heat treatment and shot peening (HT + SP). Redrawn from ref. [100].

Although the effects of statistical populations of defects on fatigue behavior are well-established for materials manufactured by conventional processes, fatigue strength prediction concerning AM materials still lacks accuracy and does not provide adequate estimation. Recently, Schneller et al. [215] developed a new methodology, based on experimental data

(residual stresses, defect population, and hardness), to assess fatigue strength of Al components with unnotched shapes. The proposed approach modifies Murakami's method [216], which correlates the fatigue resistance σ_f to the characteristic dimension of defects and material hardness HV by introducing a residual stress factor σ_r . The equation is the following:

$$\sigma_f = \sqrt{\frac{\sigma_r^2}{4} + \left(C_1 \frac{HV + C_2 S}{\sqrt{area_{eff}}^{1/6}} \right)^2} - \frac{\sigma_r}{2} \quad (3)$$

where $s = 1 - \sigma_r/HV$ is a reduction factor, $(area_{eff})^{1/2}$ is the dimension of killer defects, $C_1 = 1.43$, and $C_2 = 120$.

The equation was validated on AlSi10Mg samples fabricated by SLM in the following conditions: as-built, after a heat treatment ($T > 300$ °C for 2 h), and after HIP ($T > 500$ °C and 100 MPa for 2 h, followed by 7 h at 160 °C).

7. Conclusions

The strong competition in the aeronautic industry for producing aircrafts with improved technical features and reduced costs requires advanced structural materials which guarantee reduced weight, improved mechanical properties, and corrosion resistance. The development of such materials needs new technologies, and AM involves specific benefits mainly related to MRO operations, minimizing the “buy-to-fly” ratio and weight reduction through TO.

Recent advances in the AM of Al alloys for aeronautic applications were described and critically discussed, highlighting current problems and perspectives. Attention was focused on some relevant issues: (i) defects typically found in AM-printed Al alloys, (ii) microstructure–properties relationships, (iii) development of novel alloys, and (iv) postprocess treatments. These topics were treated by considering different AM technologies and the effects of material (powders or wires) characteristics and process parameters.

From this study, the following topics seem of particular interest for future investigations:

- (i) A major part of the literature papers are focused on specific aspects of the AM process of Al alloys; however, defects in printed components depend in many ways on material composition and process parameters, and it is a challenging task to find the optimal trade-off of all the factors affecting the final macro- and microstructure. Therefore, more efforts should be made to investigate the process of a single material in a whole by combining experimental work and simulation, with particular attention to the contributions which could be given today by artificial intelligence.
- (ii) The development of models and deep learning systems able to predict with accuracy the final characteristics of printed products will be very useful to reduce long and expensive experimental trails and accelerate the application of AM on a larger industrial scale.
- (iii) Since AM has characteristics completely different from conventional manufacturing methods, the design and development of new alloys, in particular high-strength Al alloys, with compositions specifically tailored for this technology, is a critical issue, and relevant advancements are expected from future research.
- (iv) It is of fundamental importance to identify inoculants that are more effective in promoting a microstructure consisting of equiaxed grains with small size and random orientation.
- (v) The integration of AM with MRO aircraft operations through the just-in-time production of components requires relatively simple machinery; thus, complex postprocess treatments represent a drawback. In addition to the production of printed components of better quality, a target of future research should be the reduction of postprocess treatments, as well as their simplification and integration.

Author Contributions: All the authors contributed to examine the literature and write the manuscript. All authors have read and agreed to the published version of the manuscript.

Funding: This research received no external funding.

Conflicts of Interest: The authors declare no conflict of interest.

Nomenclature

AM	Additive Manufacturing
TO	Topology Optimization
CAD	Computer-Aided Design
MRO	Maintenance, Repair, and Overhaul
L-PBF	Laser Powder Bed Fusion
DED	Direct Energy Deposition
WAAM	Wire Arc Additive Manufacturing
SLM	Selective Laser Melting
DMLS	Direct Metal Laser Sintering
CET	Columnar to Equiaxed Transition
G	Thermal gradient
R	Growth rate
EBM	Electron Beam Melting
SMS	Solidification Microstructure Selection
GND	Geometrical Necessary Dislocations
E	Dynamic modulus
YS	Yield Stress
UTS	Ultimate Tensile Strength
SP	Shot Peening
HIP	Hot Isostatic Pressing

References

- Campbell, F.C. *Manufacturing Technology for Aerospace Structural Materials*; Elsevier: Amsterdam, The Netherlands, 2006.
- Zhang, X.; Chen, Y.; Hu, J. Recent advances in the development of aerospace materials. *Prog. Aerosp. Sci.* **2018**, *97*, 22–34. [[CrossRef](#)]
- Dursun, T.; Soutis, C. Recent developments in advanced aircraft aluminium alloys. *Mater. Des.* **2014**, *56*, 862–871. [[CrossRef](#)]
- Gloria, A.; Montanari, R.; Richetta, M.; Varone, A. Alloys for aeronautic applications: State of art and perspectives. *Metals* **2019**, *9*, 662. [[CrossRef](#)]
- Debnath, B.; Shakur, M.S.; Tanjum, F.; Rahman, M.A.; Adnan, Z.H. Impact of Additive Manufacturing on the Supply Chain of Aerospace Spare Parts Industry—A Review. *Logistics* **2022**, *6*, 28. [[CrossRef](#)]
- Bendsøe, M.; Sigmund, O. *Topology Optimization: Theory, Method and Applications*; Springer: Berlin/Heidelberg, Germany, 2003.
- Fetisov, K.V.; Maksimov, P.V. Topology Optimization and Laser Additive Manufacturing in Design Process of Efficiency Lightweight Aerospace Parts. *J. Phys. Conf. Ser.* **2018**, *1015*, 052006. [[CrossRef](#)]
- Kladovasilakis, N.; Tsongas, K.; Karalekas, D.; Tzetzis, D. Architected Materials for Additive Manufacturing: A Comprehensive Review. *Materials* **2022**, *15*, 5919. [[CrossRef](#)] [[PubMed](#)]
- Costanza, G.; Gusmano, G.; Montanari, R.; Tata, M.E. Optimisation of TiH₂, and SiC content in Al foams. *Metall. Ital.* **2005**, *97*, 41–47.
- Costanza, G.; Gusmano, G.; Montanari, R.; Tata, M.E.; Ucciardello, N. Effect of powder mix composition on Al foam morphology. *J. Mater. Des. Appl.* **2008**, *222*, 131–140. [[CrossRef](#)]
- Lapi, G.; Montanari, R.; Tata, M.E.; Barbieri, G.; Balijepalli, S.K.; Kaciulis, S. Investigation of Skin-Core Joints in Aluminium Foam Sandwich Panels by EDS and XPS. *Surf. Interface Anal.* **2016**, *48*, 479–482. [[CrossRef](#)]
- Guo, N.; Leu, M.C. Additive Manufacturing: Technology, Applications and Research Needs. *Front. Mech. Eng.* **2013**, *8*, 215–243. [[CrossRef](#)]
- Singamneni, S.; Yifan, L.V.; Hewitt, A.; Chalk, R.; Thomas, W.; Jordison, D. Additive Manufacturing for the Aircraft Industry: A Review. *J. Aeronaut. Aerosp. Eng.* **2019**, *8*, 215. [[CrossRef](#)]
- Blakey-Milner, B.; Gradl, P.; Snedden, G.; Brooks, M.; Pitot, J.; Lopez, E.; Leary, M.; Berto, F.; du Plessis, A. Metal additive manufacturing in aerospace: A review. *Mater. Des.* **2021**, *209*, 110008. [[CrossRef](#)]
- Huang, R.; Riddle, M.; Graziano, D.; Warren, J.; Das, S.; Nimbalkar, S.; Cresko, J.; Masanet, E. Energy and emissions saving potential of additive manufacturing: The case of lightweight aircraft components. *J. Clean. Prod.* **2016**, *135*, 1559–1570. [[CrossRef](#)]
- Khajavi, S.H.; Partanen, J.; Holmström, J. Additive Manufacturing in the Spare Parts Supply Chain. *Comput. Ind.* **2014**, *65*, 50–63. [[CrossRef](#)]

17. Additive Manufacturing Reduces Tooling Cost and Lead Time to Produce Composite Aerospace Parts-Global Print Monitor. Available online: <http://globalprintmonitor.de/en/3d/3d-printing-news/aerospace/17617-additive-manufacturing-reducestooling-cost-and-lead-time-to-produce-composite-aerospace-parts> (accessed on 13 March 2022).
18. Lewandowski, J.J.; Seifi, M. Metal additive manufacturing: A review of mechanical properties. *Annu. Rev. Mater. Res.* **2016**, *46*, 151–186. [CrossRef]
19. Seifi, M.; Gorelik, M.; Waller, J.; Hrabec, N.; Shamsaei, N.; Daniewicz, S.; Lewandowski, J.J. Progress towards metal additive manufacturing standardization to support qualification and certification. *JOM* **2017**, *69*, 439–455. [CrossRef]
20. Li, P.; Warner, D.H.; Fatemi, A.; Phan, N. Critical assessment of the fatigue performance of additively manufactured Ti–6Al–4V and perspective for future research. *Int. J. Fatigue* **2016**, *85*, 130–143. [CrossRef]
21. Fatemi, A.; Molaei, R.; Sharifimehr, S.; Shamsaei, N.; Phan, N. Torsional fatigue behavior of wrought and additive manufactured Ti–6Al–4V by powder bed fusion including surface finish effect. *Int. J. Fatigue* **2017**, *99*, 187–201. [CrossRef]
22. Yadroitsev, I.; Yadroitsava, I.; du Plessis, A.; MacDonald, E. *Fundamentals of Laser Powder Bed Fusion of Metals*, 1st ed.; Elsevier: Amsterdam, The Netherlands, 2021.
23. Gisario, A.; Kazarian, M.; Martina, F.; Mehrpouya, M. Metal Additive Manufacturing in the Commercial Aviation Industry: A Review. *J. Manuf. Syst.* **2019**, *53*, 124–149. [CrossRef]
24. Kotadia, H.R.; Gibbons, G.; Das, A.; Howes, P.D. A review of Laser Powder Bed Fusion Additive Manufacturing of aluminium alloys: Microstructure and properties. *Addit. Manuf.* **2021**, *46*, 102155. [CrossRef]
25. Madhavadas, V.; Srivastava, D.; Chadha, U.; Aravind Raj, S.; Sultan, M.T.H.; Shahar, F.S.; Shah, A.U.M. A Review on Metal Additive Manufacturing for Intricately Shaped Aerospace Components. *CIRP J. Manuf. Sci. Technol.* **2022**, *39*, 18–36. [CrossRef]
26. Najmon, J.C.; Raeisi, S.; Tovar, A. *Additive Manufacturing for the Aerospace Industry*; Froes, F., Boyer, R., Eds.; Elsevier: Amsterdam, The Netherlands, 2019; pp. 7–31. [CrossRef]
27. Make Parts Fast. Available online: <https://www.makepartsfast.com/additive-manufacturing-enables-bionic-aircraft-designs/> (accessed on 17 January 2023).
28. AdditiveManufacturing. Available online: <https://additivemanufacturing.com/2017/04/10/norsk-titanium-to-deliver-the-worlds-first-faa-approved-3d-printed-structural-titanium-components-to-boeing/> (accessed on 17 January 2023).
29. Airbus. Available online: <https://www.airbus.com/en/newsroom/press-releases/2017-09-first-titanium-3d-printed-part-installed-into-serial-production> (accessed on 17 January 2023).
30. GKN Aerospace. Available online: <https://www.gknaerospace.com/en/our-technology/2017/gkn-aerospace-engine-systems-journey-to-introduce-additive-manufacturing/> (accessed on 17 January 2023).
31. EOS. Available online: <https://www.eos.info/en/all-3d-printing-applications/aerospace-3d-printing/aircraft> (accessed on 17 January 2023).
32. Autodesk. Available online: <https://adsknews.autodesk.com/stories/how-this-light-weight-airplane-seat-can-save-airlines-200000000-and-dramatically-reduce-carbon-emissions> (accessed on 17 January 2023).
33. Arch Daily. Available online: <https://www.archdaily.com/780661/the-livings-parametric-3d-printed-airplane-partition-is-designed-to-mimic-bone-structure> (accessed on 17 January 2023).
34. EOS. Available online: <https://www.eos.info/en/innovations/all-3d-printing-applications/aerospace/aerospace-case-studies/ruag-aerospace-3d-printed-satellite-components> (accessed on 17 January 2023).
35. Additive Manufacturing Media. Available online: <https://www.additivemanufacturing.media/articles/what-is-the-role-for-additive-manufacturing-in-aircraft-structural-components> (accessed on 17 January 2023).
36. EOS. Available online: https://www.eos.info/01_parts-and-applications/case_studies_applications_parts/_case_studies_pdf/en_cases/cs_m_aerospace_sogeti_en.pdf (accessed on 17 January 2023).
37. Hettesheimer, T.; Hirzel, S.; Roß, H.B. Energy savings through additive manufacturing: An analysis of selective laser sintering for automotive and aircraft components. *Energy Effic.* **2018**, *11*, 1227–1245. [CrossRef]
38. nTopology. Available online: <https://ntopology.com/case-studies/cobra-aero/> (accessed on 17 January 2023).
39. Muhammad, M.; Nezhadfar, P.D.; Thompson, S.; Saharan, A.; Phan, N.; Shamsaei, N. A comparative investigation on the microstructure and mechanical properties of additively manufactured aluminum alloys. *Int. J. Fatigue* **2021**, *146*, 106165. [CrossRef]
40. Aboulkhair, N.T.; Simonelli, M.; Parry, L.; Ashcroft, I.; Tuck, C.; Hague, R. 3D printing of aluminium alloys: Additive manufacturing of aluminium alloys using selective laser melting. *Prog. Mater. Sci.* **2019**, *106*, 100578. [CrossRef]
41. Altıparmak, S.C.; Yardley, V.A.; Shi, Z.; Lin, J. Challenges in additive manufacturing of high-strength aluminium alloys and current developments in hybrid additive manufacturing. *Int. J. Lightweight Mater. Manuf.* **2021**, *4*, 246–261. [CrossRef]
42. Waller, D.; Polizzi, A.; Iten, J. Feasibility study of additively manufactured Al-6061 RAM2 parts for aerospace applications. In Proceedings of the AIAA 2019-0409, Session: Materials and Design for Additive Manufacturing, San Diego, CA, USA, 7–11 January 2019. [CrossRef]
43. DebRoy, T.; Wei, H.L.; Zuback, J.S.; Mukherjee, T.; Elmer, J.W.; Milewski, J.O.; Beese, A.M.; Wilson-Heid, A.; De, A.; Zhang, W. Additive Manufacturing of Metallic Components—Process, Structure and Properties. *Prog. Mater. Sci.* **2018**, *92*, 112–224. [CrossRef]
44. Aboulkhair, N.T.; Everitt, N.M.; Maskery, I.; Ashcroft, I.; Tuck, C. Selective laser melting of aluminum alloys. *MRS Bull.* **2017**, *42*, 311–319. [CrossRef]

45. Aversa, A.; Marchese, G.; Saboori, A.; Bassini, E.; Manfredi, D.; Biamino, S.; Ugues, D.; Fino, P.; Lombardi, M. New Aluminum Alloys Specifically Designed for Laser Powder Bed Fusion: A Review. *Materials* **2019**, *12*, 1007. [[CrossRef](#)]
46. Louvis, E.; Fox, P.; Sutcliffe, C.J. Selective laser melting of aluminium components. *J. Mater. Process. Technol.* **2011**, *211*, 275–284. [[CrossRef](#)]
47. Buchbinder, D.; Schleifenbaum, H.; Heidrich, S.; Meiners, W.; Bültmann, J. High Power Selective Laser Melting (HP SLM) of Aluminum Parts. *Phys. Procedia* **2011**, *12*, 271–278. [[CrossRef](#)]
48. Hamidi Nasab, M.; Romano, S.; Gastaldi, D.; Beretta, S.; Vedani, M. Combined effect of surface anomalies and volumetric defects on fatigue assessment of AlSi7Mg fabricated via laser powder bed fusion. *Addit. Manuf.* **2020**, *34*, 100918. [[CrossRef](#)]
49. Bauer, D.M.; Dietrich, K.; Walter, M.; Forêt, P.; Palm, F.; Witt, G. Effect of process gas and powder quality on aluminum alloys processed by laser based powder bed melting process. In Proceedings of the 27th Annual International Solid Freeform Fabrication Symposium—An Additive Manufacturing Conference, Austin, TX, USA, 8–10 August 2016; pp. 419–425.
50. Anwar, A.B.; Pham, Q.C. Selective laser melting of AlSi10Mg: Effects of scan direction, part placement and inert gas flow velocity on tensile strength. *J. Mater. Process. Technol.* **2017**, *240*, 388–396. [[CrossRef](#)]
51. Galy, C.; Le Guen, E.; Lacoste, E.; Arvieu, C. Main defects observed in aluminum alloy parts produced by SLM: From causes to consequences. *Addit. Manuf.* **2018**, *22*, 165–175. [[CrossRef](#)]
52. Kimura, T.; Nakamoto, T. Microstructures and mechanical properties of A356 (AlSi7Mg0.3) aluminum alloy fabricated by selective laser melting. *Mater. Des.* **2016**, *89*, 1294–1301. [[CrossRef](#)]
53. Read, N.; Wang, W.; Essa, K.; Attallah, M.M. Selective Laser Melting of AlSi10Mg Alloy: Process Optimisation and Mechanical Properties Development. *Mater. Des.* **2015**, *65*, 417–424. [[CrossRef](#)]
54. Damon, J.; Dietrich, S.; Vollert, F.; Gibmeier, J.; Schulze, V. Process Dependent Porosity and the Influence of Shot Peening on Porosity Morphology Regarding Selective Laser Melted AlSi10Mg Parts. *Addit. Manuf.* **2018**, *20*, 77–89. [[CrossRef](#)]
55. Cerri, E.; Ghio, E.; Bolelli, G. Defect-Related Vickers Microhardness of Al-Si-Mg Alloy Manufactured by Laser Powder Bed Fusion with Post-process Heat Treatments. *J. Mater. Eng. Perform.* **2021**, *31*, 8047–8067. [[CrossRef](#)]
56. Hauser, T.; Reisch, R.T.; Breese, P.P.; Lutz, B.S.; Pantano, M.; Nalam, Y.; Bela, K.; Kamps, T.; Volpp, J.; Kaplan, A.F.H. Porosity in Wire Arc Additive Manufacturing of Aluminium Alloys. *Addit. Manuf.* **2021**, *41*, 101993. [[CrossRef](#)]
57. Aboulkhair, N.T.; Everitt, N.M.; Ashcroft, I.; Tuck, C. Reducing Porosity in AlSi10Mg Parts Processed by Selective Laser Melting. *Addit. Manuf.* **2014**, *1–4*, 77–86. [[CrossRef](#)]
58. Tonelli, L.; Liverani, E.; Valli, G.; Fortunato, A.; Ceschini, L. Effects of Powders and Process Parameters on Density and Hardness of A357 Aluminum Alloy Fabricated by Selective Laser Melting. *Int. J. Adv. Manuf. Technol.* **2020**, *106*, 371–383. [[CrossRef](#)]
59. Maamoun, A.H.; Elbestawi, M.; Dosbaeva, G.K.; Veldhuis, S.C. Thermal Post-Processing of AlSi10Mg Parts Produced by Selective Laser Melting Using Recycled Powder. *Addit. Manuf.* **2018**, *21*, 234–247. [[CrossRef](#)]
60. Stopyra, W.; Gruber, K.; Smolina, I.; Kurzynowski, T.; Kuźnicka, B. Laser Powder Bed Fusion of AA7075 Alloy: Influence of Process Parameters on Porosity and Hot Cracking. *Addit. Manuf.* **2020**, *35*, 101270. [[CrossRef](#)]
61. Muñoz-Lerma, J.A.; Nommeots-Nomm, A.; Waters, K.E.; Brochu, M. A Comprehensive Approach to Powder Feedstock Characterization for Powder Bed Fusion Additive Manufacturing: A Case Study on AlSi7Mg. *Materials* **2018**, *11*, 2386. [[CrossRef](#)] [[PubMed](#)]
62. Baitimerov, R.; Lykov, P.; Zhrebtsov, D.; Radionova, L.; Shults, A.; Prashanth, K.G. Influence of Powder Characteristics on Processability of AlSi12 Alloy Fabricated by Selective Laser Melting. *Materials* **2018**, *11*, 742. [[CrossRef](#)]
63. Balbaa, M.A.; Ghasemi, A.; Fereiduni, E.; Elbestawi, M.A.; Jadhav, S.D.; Kruth, J.-P. Role of Powder Particle Size on Laser Powder Bed Fusion Processability of AlSi10mg Alloy. *Addit. Manuf.* **2021**, *37*, 101630. [[CrossRef](#)]
64. Riener, K.; Albrecht, N.; Ziegelmeier, S.; Ramakrishnan, R.; Haferkamp, L.; Spierings, A.B.; Leichtfried, G.J. Influence of Particle Size Distribution and Morphology on the Properties of the Powder Feedstock as Well as of AlSi10Mg Parts Produced by Laser Powder Bed Fusion (LPBF). *Addit. Manuf.* **2020**, *34*, 101286. [[CrossRef](#)]
65. Weingarten, C.; Buchbinder, D.; Pirch, N.; Meiners, W.; Wissenbach, K.; Poprawe, R. Formation and Reduction of Hydrogen Porosity during Selective Laser Melting of AlSi10Mg. *J. Mater. Process. Technol.* **2015**, *221*, 112–120. [[CrossRef](#)]
66. Li, X.P.; O'Donnell, K.M.; Sercombe, T.B. Selective Laser Melting of Al-12Si Alloy: Enhanced Densification via Powder Drying. *Addit. Manuf.* **2016**, *10*, 10–14. [[CrossRef](#)]
67. Thijs, L.; Kempen, K.; Kruth, J.-P.; Van Humbeeck, J. Fine-Structured Aluminium Products with Controllable Texture by Selective Laser Melting of Pre-Alloyed AlSi10Mg Powder. *Acta Mater.* **2013**, *61*, 1809–1819. [[CrossRef](#)]
68. Montero-Sistiaga, M.L.; Mertens, R.; Vrancken, B.; Wang, X.; Van Hooreweder, B.; Kruth, J.-P.; Van Humbeeck, J. Changing the Alloy Composition of Al7075 for Better Processability by Selective Laser Melting. *J. Mater. Process. Technol.* **2016**, *238*, 437–445. [[CrossRef](#)]
69. Kaufmann, N.; Imran, M.; Wischeropp, T.M.; Emmelmann, C.; Siddique, S.; Walther, F. Influence of Process Parameters on the Quality of Aluminium Alloy EN AW 7075 Using Selective Laser Melting (SLM). *Phys. Procedia* **2016**, *83*, 918–926. [[CrossRef](#)]
70. Martin, J.H.; Yahata, B.D.; Hundley, J.M.; Mayer, J.A.; Schaedler, T.A.; Pollock, T.M. 3D Printing of High-Strength Aluminium Alloys. *Nature* **2017**, *549*, 365–369. [[CrossRef](#)]
71. Griffiths, S.; Croteau, J.R.; Rossell, M.D.; Erni, R.; De Luca, A.; Vo, N.Q.; Dunand, D.C.; Leinenbach, C. Coarsening- and Creep Resistance of Precipitation-Strengthened Al-Mg-Zr Alloys Processed by Selective Laser Melting. *Acta Mater.* **2020**, *188*, 192–202. [[CrossRef](#)]

72. Zhang, H.; Zhu, H.; Nie, X.; Yin, J.; Hu, Z.; Zeng, X. Effect of Zirconium Addition on Crack, Microstructure and Mechanical Behavior of Selective Laser Melted Al-Cu-Mg Alloy. *Scr. Mater.* **2017**, *134*, 6–10. [[CrossRef](#)]
73. Spierings, A.B.; Dawson, K.; Heeling, T.; Uggowitzer, P.J.; Schäublin, R.; Palm, F.; Wegener, K. Microstructural features of Sc and Zr-modified Al-Mg alloys processed by selective laser melting. *Mater. Des.* **2017**, *115*, 52–63. [[CrossRef](#)]
74. Zhou, L.; Hyer, H.; Park, S.; Pan, H.; Bai, Y.; Rice, K.P.; Sohn, Y. Microstructure and Mechanical Properties of Zr-Modified Aluminum Alloy 5083 Manufactured by Laser Powder Bed Fusion. *Addit. Manuf.* **2019**, *28*, 485–496. [[CrossRef](#)]
75. Zhou, L.; Pan, H.; Hyer, H.; Park, S.; Bai, Y.; McWilliams, B.; Cho, K.; Sohn, Y. Microstructure and Tensile Property of a Novel AlZnMgScZr Alloy Additively Manufactured by Gas Atomization and Laser Powder Bed Fusion. *Scr. Mater.* **2019**, *158*, 24–28. [[CrossRef](#)]
76. Bi, J.; Zhenglong, L.; Chen, Y.; Chen, X.; Tian, Z.; Liang, J.; Zhang, X.; Qin, X. Microstructure and Mechanical Properties of a Novel Sc and Zr Modified 7075 Aluminum Alloy Prepared by Selective Laser Melting. *Mater. Sci. Eng. A* **2019**, *768*, 138478. [[CrossRef](#)]
77. Hu, Z.; Nie, X.; Qi, Y.; Zhang, H.; Zhu, H. Cracking Criterion for High Strength Al-Cu Alloys Fabricated by Selective Laser Melting. *Addit. Manuf.* **2021**, *37*, 101709. [[CrossRef](#)]
78. Cao, Y.; Wei, H.L.; Yang, T.; Liu, T.T.; Liao, W.H. Printability Assessment with Porosity and Solidification Cracking Susceptibilities for a High Strength Aluminum Alloy during Laser Powder Bed Fusion. *Addit. Manuf.* **2021**, *46*, 102103. [[CrossRef](#)]
79. Zhang, H.; Zhu, H.; Qi, T.; Hu, Z.; Zeng, X. Selective Laser Melting of High Strength Al-Cu-Mg Alloys: Processing, Microstructure and Mechanical Properties. *Mater. Sci. Eng. A* **2016**, *656*, 47–54. [[CrossRef](#)]
80. Qi, Y.; Zhang, H.; Xiaojia, N.; Hu, Z.; Zhu, H.; Zeng, X. A High Strength Al-Li Alloy Produced by Laser Powder Bed Fusion: Densification, Microstructure, and Mechanical Properties. *Addit. Manuf.* **2020**, *35*, 101346. [[CrossRef](#)]
81. Wang, P.; Gammer, C.; Brenne, F.; Prashanth, K.G.; Mendes, R.G.; Rummeli, M.H.; Gemming, T.; Eckert, J.; Scudino, S. Microstructure and Mechanical Properties of a Heat-Treatable Al-3.5Cu-1.5Mg-1Si Alloy Produced by Selective Laser Melting. *Mater. Sci. Eng. A* **2018**, *711*, 562–570. [[CrossRef](#)]
82. Nie, X.; Zhang, H.; Zhu, H.; Hu, Z.; Ke, L.; Zeng, X. Effect of Zr Content on Formability, Microstructure and Mechanical Properties of Selective Laser Melted Zr Modified Al-4.24Cu-1.97Mg-0.56Mn Alloys. *J. Alloys Compd.* **2018**, *764*, 977–986. [[CrossRef](#)]
83. Rasch, M.; Heberle, J.; Dechet, M.A.; Bartels, D.; Gotterbarm, M.R.; Klein, L.; Gorunov, A.; Schmidt, J.; Körner, C.; Peukert, W.; et al. Grain Structure Evolution of Al-Cu Alloys in Powder Bed Fusion with Laser Beam for Excellent Mechanical Properties. *Materials* **2020**, *13*, 82. [[CrossRef](#)]
84. Rosenthal, D. Mathematical theory of heat distribution during welding and cutting. *Weld. J.* **1941**, *20*, 220–234.
85. Kok, Y.; Tan, X.P.; Wang, P.; Nai, M.L.S.; Loh, N.H.; Liu, E.; Tor, S.B. Anisotropy and heterogeneity of microstructure and mechanical properties in metal additive manufacturing: A critical review. *Mater. Des.* **2018**, *139*, 565–586. [[CrossRef](#)]
86. Suryawanshi, J.; Prashanth, K.G.; Scudino, S.; Eckert, J.; Prakash, O.; Ramamurty, U. Simultaneous enhancements of strength and toughness in an Al-12Si alloy synthesized using selective laser melting. *Acta Mater.* **2016**, *115*, 285–294. [[CrossRef](#)]
87. Kempen, K.; Thijs, L.; Van Humbeeck, J.; Kruth, J.-P. Mechanical Properties of AlSi10Mg Produced by Selective Laser Melting. *Phys. Procedia* **2012**, *39*, 439–446. [[CrossRef](#)]
88. Manfredi, D.; Calignano, F.; Krishnan, M.; Canali, R.; Ambrosio, E.P.; Atzeni, E. From Powders to Dense Metal Parts: Characterization of a Commercial AlSiMg Alloy Processed through Direct Metal Laser Sintering. *Materials* **2013**, *6*, 856–869. [[CrossRef](#)]
89. Rashid, R.; Masood, S.H.; Ruan, D.; Palanisamy, S.; Rahman Rashid, R.A.; Elambasseril, J.; Brandt, M. Effect of energy per layer on the anisotropy of selective laser melted AlSi12 aluminium alloy. *Addit. Manuf.* **2018**, *22*, 426–439. [[CrossRef](#)]
90. Nezhadfar, P.D.; Thompson, S.; Saharan, A.; Phan, N.; Shamsaei, N. Structural Integrity of Additively Manufactured Aluminum Alloys: Effects of Build Orientation on Microstructure, Porosity, and Fatigue Behavior. *Addit. Manuf.* **2021**, *47*, 102292. [[CrossRef](#)]
91. Chen, Y.; Zhang, J.; Gu, X.; Dai, N.; Qin, P.; Zhang, L.-C. Distinction of Corrosion Resistance of Selective Laser Melted Al-12Si Alloy on Different Planes. *J. Alloys Compd.* **2018**, *747*, 648–658. [[CrossRef](#)]
92. Tonelli, L.; Laghi, V.; Palermo, M.; Trombetti, T.; Ceschini, L. AA5083 (Al-Mg) Plates Produced by Wire-and-Arc Additive Manufacturing: Effect of Specimen Orientation on Microstructure and Tensile Properties. *Prog. Addit. Manuf.* **2021**, *6*, 479–494. [[CrossRef](#)]
93. Qin, Z.; Kang, N.; El Mansori, M.; Wang, Z.; Wang, H.; Lin, X.; Chen, J.; Huang, W. Anisotropic High Cycle Fatigue Property of Sc and Zr-Modified Al-Mg Alloy Fabricated by Laser Powder Bed Fusion. *Addit. Manuf.* **2022**, *49*, 102514. [[CrossRef](#)]
94. Majeed, A.; Ahmed, A.; Salam, A.; Sheikh, M.Z. Surface Quality Improvement by Parameters Analysis, Optimization and Heat Treatment of AlSi10Mg Parts Manufactured by SLM Additive Manufacturing. *Int. J. Lightweight Mater. Manuf.* **2019**, *2*, 288–295. [[CrossRef](#)]
95. Mohammadi, M.; Asgari, H. Achieving Low Surface Roughness AlSi10Mg 200C Parts Using Direct Metal Laser Sintering. *Addit. Manuf.* **2018**, *20*, 23–32. [[CrossRef](#)]
96. Poncelet, O.; Marteleur, M.; van der Rest, C.; Rigo, O.; Adrien, J.; Dancette, S.; Jacques, P.J.; Simar, A. Critical Assessment of the Impact of Process Parameters on Vertical Roughness and Hardness of Thin Walls of AlSi10Mg Processed by Laser Powder Bed Fusion. *Addit. Manuf.* **2021**, *38*, 101801. [[CrossRef](#)]
97. Calignano, F.; Manfredi, D.; Ambrosio, E.P.; Iuliano, L.; Fino, P. Influence of Process Parameters on Surface Roughness of Aluminum Parts Produced by DMLS. *Int. J. Adv. Manuf. Technol.* **2013**, *67*, 2743–2751. [[CrossRef](#)]
98. Hönnige, J.R.; Colegrove, P.A.; Ganguly, S.; Eimer, E.; Kabra, S.; Williams, S. Control of Residual Stress and Distortion in Aluminium Wire + Arc Additive Manufacture with Rolling. *Addit. Manuf.* **2018**, *22*, 775–783. [[CrossRef](#)]

99. Wang, L.; Jiang, X.; Zhu, Y.; Ding, Z.; Zhu, X.; Sun, J.; Yan, B. Investigation of Performance and Residual Stress Generation of AlSi10Mg Processed by Selective Laser Melting. *Adv. Mater. Sci. Eng.* **2018**, *2018*, 7814039. [[CrossRef](#)]
100. Salmi, A.; Atzeni, E.; Iuliano, L.; Galati, M. Experimental Analysis of Residual Stresses on AlSi10Mg Parts Produced by Means of Selective Laser Melting (SLM). *Procedia CIRP* **2017**, *62*, 458–463. [[CrossRef](#)]
101. Kempen, K.; Thijs, L.; Yasa, E.; Badrossamay, M.; Verheecke, W.; Kruth, J. Process Optimization and Microstructural Analysis for Selective Laser Melting of AlSi10Mg. In Proceedings of the 22nd Annual International Solid Freeform Fabrication Symposium—An Additive Manufacturing Conference, SFF 2011, Austin, TX, USA, 8–10 August 2011.
102. Buchbinder, D.; Meiners, W.; Pirch, N.; Wissenbach, K.; Schrage, J. Investigation on Reducing Distortion by Preheating during Manufacture of Aluminum Components Using Selective Laser Melting. *J. Laser Appl.* **2014**, *26*, 012004. [[CrossRef](#)]
103. Oyama, K.; Diplas, S.; M'hamdi, M.; Gunnæs, A.E.; Azar, A.S. Heat Source Management in Wire-Arc Additive Manufacturing Process for Al-Mg and Al-Si Alloys. *Addit. Manuf.* **2019**, *26*, 180–192. [[CrossRef](#)]
104. Liu, Y.J.; Liu, Z.; Jiang, Y.; Wang, G.W.; Yang, Y.; Zhang, L.C. Gradient in Microstructure and Mechanical Property of Selective Laser Melted AlSi10Mg. *J. Alloys Compd.* **2018**, *735*, 1414–1421. [[CrossRef](#)]
105. Liu, X.; Zhao, C.; Zhou, X.; Shen, Z.; Liu, W. Microstructure of Selective Laser Melted AlSi10Mg Alloy. *Mater. Des.* **2019**, *168*, 107677. [[CrossRef](#)]
106. Hadadzadeh, A.; Shalchi Amirkhiz, B.; Odeshi, A.G.; Li, J.; Mohammadi, M. Role of Hierarchical Microstructure of Additively Manufactured AlSi10Mg on Dynamic Loading Behavior. *Addit. Manuf.* **2019**, *28*, 1–13. [[CrossRef](#)]
107. Tonelli, L. Revealing the Hierarchical Microstructure of Innovative Additively Manufactured Metal Parts with Conventional Light Microscopy. *Metallogr. Microstruct. Anal.* **2021**, *10*, 278–282. [[CrossRef](#)]
108. Xiong, Z.H.; Liu, S.L.; Li, S.F.; Shi, Y.; Yang, Y.F.; Misra, R.D.K. Role of Melt Pool Boundary Condition in Determining the Mechanical Properties of Selective Laser Melting AlSi10Mg Alloy. *Mater. Sci. Eng. A* **2019**, *740–741*, 148–156. [[CrossRef](#)]
109. Cabibbo, M.; Montanari, R.; Pola, A.; Tocci, M.; Varone, A. Mechanical Spectroscopy Study of As-Cast and Additive Manufactured AlSi10Mg. *J. Alloys Compd.* **2022**, *914*, 165361. [[CrossRef](#)]
110. Zhou, L.; Mehta, A.; Schulz, E.; McWilliams, B.; Cho, K.; Sohn, Y. Microstructure, Precipitates and Hardness of Selectively Laser Melted AlSi10Mg Alloy before and after Heat Treatment. *Mater. Charact.* **2018**, *143*, 5–17. [[CrossRef](#)]
111. Hadadzadeh, A.; Amirkhiz, B.S.; Mohammadi, M. Contribution of Mg₂Si Precipitates to the Strength of Direct Metal Laser Sintered AlSi10Mg. *Mater. Sci. Eng. A* **2019**, *739*, 295–300. [[CrossRef](#)]
112. Wu, J.; Wang, X.Q.; Wang, W.; Attallah, M.M.; Loretto, M.H. Microstructure and Strength of Selectively Laser Melted AlSi10Mg. *Acta Mater.* **2016**, *117*, 311–320. [[CrossRef](#)]
113. Hadadzadeh, A.; Amirkhiz, B.S.; Langelier, B.; Li, J.; Mohammadi, M. Microstructural Consistency in the Additive Manufactured Metallic Materials: A Study on the Laser Powder Bed Fusion of AlSi10Mg. *Addit. Manuf.* **2021**, *46*, 102166. [[CrossRef](#)]
114. Fite, J.; Eswarappa Prameela, S.; Slotwinski, J.A.; Weihs, T.P. Evolution of the Microstructure and Mechanical Properties of Additively Manufactured AlSi10Mg during Room Temperature Holds and Low Temperature Aging. *Addit. Manuf.* **2020**, *36*, 101429. [[CrossRef](#)]
115. Ghio, E.; Cerri, E. Additive Manufacturing of AlSi10Mg and Ti6Al4V Lightweight Alloys via Laser Powder Bed Fusion: A Review of Heat Treatments Effects. *Materials* **2022**, *15*, 2047. [[CrossRef](#)]
116. Kurz, W.; Bezençon, C.; Gäumann, M. Columnar to Equiaxed Transition in Solidification Processing. *Sci. Technol. Adv. Mater.* **2001**, *2*, 185–191. [[CrossRef](#)]
117. Montiel, D.; Liu, L.; Xiao, L.; Zhou, Y.; Provas, N. Microstructure Analysis of AZ31 Magnesium Alloy Welds Using Phase-Field Models. *Acta Mater.* **2012**, *60*, 5925–5932. [[CrossRef](#)]
118. Yang, K.V.; Shi, Y.; Palm, F.; Wu, X.; Rometsch, P. Columnar to Equiaxed Transition in Al-Mg(-Sc)-Zr Alloys Produced by Selective Laser Melting. *Scr. Mater.* **2018**, *145*, 113–117. [[CrossRef](#)]
119. Rao, H.; Giet, S.; Yang, K.; Wu, X.; Davies, C.H.J. The Influence of Processing Parameters on Aluminium Alloy A357 Manufactured by Selective Laser Melting. *Mater. Des.* **2016**, *109*, 334–346. [[CrossRef](#)]
120. Wang, Z.; Wang, X.; Chen, X.; Qiu, C. Complete Columnar-to-Equiaxed Transition and Significant Grain Refinement in an Aluminium Alloy by Adding Nb Particles through Laser Powder Bed Fusion. *Addit. Manuf.* **2022**, *51*, 102615. [[CrossRef](#)]
121. Li, X.P.; Ji, G.; Chen, Z.; Addad, A.; Wu, Y.; Wang, H.W.; Vleugels, J.; Van Humbeeck, J.; Kruth, J.P. Selective Laser Melting of Nano-TiB₂ Decorated AlSi10Mg Alloy with High Fracture Strength and Ductility. *Acta Mater.* **2017**, *129*, 183–193. [[CrossRef](#)]
122. Spierings, A.B.; Dawson, K.; Dumitraschkewitz, P.; Pogatscher, S.; Wegener, K. Microstructure Characterization of SLM-Processed Al-Mg-Sc-Zr Alloy in the Heat Treated and HIPed Condition. *Addit. Manuf.* **2018**, *20*, 173–181. [[CrossRef](#)]
123. Hadadzadeh, A.; Amirkhiz, B.S.; Li, J.; Mohammadi, M. Columnar to Equiaxed Transition during Direct Metal Laser Sintering of AlSi10Mg Alloy: Effect of Building Direction. *Addit. Manuf.* **2018**, *23*, 121–131. [[CrossRef](#)]
124. Maizza, G.; Pero, R.; Richetta, M.; Montanari, R. Continuous Dynamic Recrystallization (CDRX) Model for Aluminum Alloys. *J. Mater. Sci.* **2018**, *53*, 4563–4573. [[CrossRef](#)]
125. Tedde, G.M.; Di Schino, A.; Donnini, R.; Montanari, R.; Richetta, M.; Santo, L.; Testani, C.; Varone, A. An Innovative Industrial Process for Forging 7050 Al Alloy. *Mater. Sci. Forum* **2019**, *941*, 1047–1052. [[CrossRef](#)]
126. Angella, G.; Di Schino, A.; Donnini, R.; Richetta, M.; Testani, C.; Varone, A. AA7050 Al Alloy Hot-Forging Process for Improved Fracture Toughness Properties. *Metals* **2019**, *9*, 64. [[CrossRef](#)]

127. Di Schino, A.; Montanari, R.; Testani, C.; Varone, A. Dislocation Breakaway Damping in AA7050 Alloy. *Metals* **2020**, *10*, 1682. [[CrossRef](#)]
128. Cong, B.; Ding, J.; Williams, S. Effect of Arc Mode in Cold Metal Transfer Process on Porosity of Additively Manufactured Al-6.3%Cu Alloy. *Int. J. Adv. Manuf. Technol.* **2015**, *76*, 1593–1606. [[CrossRef](#)]
129. Bai, J.Y.; Yang, C.L.; Lin, S.B.; Dong, B.L.; Fan, C.L. Mechanical Properties of 2219-Al Components Produced by Additive Manufacturing with TIG. *Int. J. Adv. Manuf. Technol.* **2016**, *86*, 479–485. [[CrossRef](#)]
130. Gu, J.; Ding, J.; Williams, S.W.; Gu, H.; Bai, J.; Zhai, Y.; Ma, P. The Strengthening Effect of Inter-Layer Cold Working and Post-Deposition Heat Treatment on the Additively Manufactured Al-6.3Cu Alloy. *Mater. Sci. Eng. A* **2016**, *651*, 18–26. [[CrossRef](#)]
131. Sun, R.; Li, L.; Zhu, Y.; Guo, W.; Peng, P.; Cong, B.; Sun, J.; Che, Z.; Li, B.; Guo, C.; et al. Microstructure, Residual Stress and Tensile Properties Control of Wire-Arc Additive Manufactured 2319 Aluminum Alloy with Laser Shock Peening. *J. Alloys Compd.* **2018**, *747*, 255–265. [[CrossRef](#)]
132. Geng, H.; Li, J.; Xiong, J.; Lin, X. Optimisation of Interpass Temperature and Heat Input for Wire and Arc Additive Manufacturing 5A06 Aluminium Alloy. *Sci. Technol. Weld. Join.* **2017**, *22*, 472–483. [[CrossRef](#)]
133. Geng, H.; Li, J.; Xiong, J.; Lin, X.; Zhang, F. Geometric Limitation and Tensile Properties of Wire and Arc Additive Manufacturing 5A06 Aluminum Alloy Parts. *J. Mater. Eng. Perform.* **2017**, *26*, 621–629. [[CrossRef](#)]
134. Gu, J.; Wang, X.; Bai, J.; Ding, J.; Williams, S.; Zhai, Y.; Liu, K. Deformation Microstructures and Strengthening Mechanisms for the Wire+arc Additively Manufactured Al-Mg4.5Mn Alloy with Inter-Layer Rolling. *Mater. Sci. Eng. A* **2018**, *712*, 292–301. [[CrossRef](#)]
135. Zhang, C.; Li, Y.; Gao, M.; Zeng, X. Wire Arc Additive Manufacturing of Al-6Mg Alloy Using Variable Polarity Cold Metal Transfer Arc as Power Source. *Mater. Sci. Eng. A* **2018**, *711*, 415–423. [[CrossRef](#)]
136. Dong, B.; Cai, X.; Lin, S.; Li, X.; Fan, C.; Yang, C.; Sun, H. Wire Arc Additive Manufacturing of Al-Zn-Mg-Cu Alloy: Microstructures and Mechanical Properties. *Addit. Manuf.* **2020**, *36*, 101447. [[CrossRef](#)]
137. Zhou, Y.; Lin, X.; Kang, N.; Tang, Y.; Huang, W.; Wang, Z. The Heterogeneous Band Microstructure and Mechanical Performance in a Wire + Arc Additively Manufactured 2219 Al Alloy. *Addit. Manuf.* **2022**, *49*, 102486. [[CrossRef](#)]
138. Tiryakioğlu, M.; Campbell, J. Ductility, Structural Quality, and Fracture Toughness of A-Cu-Mg-Ag (A201) Alloy Castings. *Mater. Sci. Technol.* **2009**, *25*, 784–789. [[CrossRef](#)]
139. Kuo, Y.S. Mechanical Properties and Porosity Content of A201 Aluminum Alloy Castings in Different Cooling Rate Sand Molds. *Adv. Mater. Res.* **2011**, *154–155*, 787–793. [[CrossRef](#)]
140. Roscher, M.; Balachandran, S.; Mayweg, D.; Jäggle, E. Development of Al-Ti-Based Alloys for Laser Powder Bed Fusion. *Addit. Manuf.* **2021**, *47*, 102315. [[CrossRef](#)]
141. Aeromet. Available online: <https://www.aeromet.co.uk/a20x> (accessed on 13 January 2023).
142. Bermingham, M.; StJohn, D.; Easton, M.; Yuan, L.; Dargusch, M. Revealing the Mechanisms of Grain Nucleation and Formation During Additive Manufacturing. *JOM* **2020**, *72*, 1065–1073. [[CrossRef](#)]
143. Carluccio, D.; Bermingham, M.J.; Zhang, Y.; StJohn, D.H.; Yang, K.; Rometsch, P.A.; Wu, X.; Dargusch, M.S. Grain Refinement of Laser Remelted Al-7Si and 6061 Aluminium Alloys with Tibor® and Scandium Additions. *J. Manuf. Process.* **2018**, *35*, 715–720. [[CrossRef](#)]
144. Ghoncheh, M.H.; Sanjari, M.; Zoeram, A.S.; Cyr, E.; Amirkhiz, B.S.; Lloyd, A.; Haghshenas, M.; Mohammadi, M. On the Microstructure and Solidification Behavior of New Generation Additively Manufactured Al-Cu-Mg-Ag-Ti-B Alloys. *Addit. Manuf.* **2021**, *37*, 101724. [[CrossRef](#)]
145. Bassani, P.; Biffi, C.A.; Casati, R.; Zanatta Alarcon, A.; Tuissi, A.; Vedani, M. Properties of Aluminium Alloys Produced by Selective Laser Melting. *Key Eng. Mater.* **2016**, *710*, 83–88. [[CrossRef](#)]
146. Tocci, M.; Varone, A.; Montanari, R.; Pola, A. Study of High Temperature Properties of AlSi10Mg Alloy Produced by Laser-Based Powder Bed Fusion. *Mater. Sci. Forum* **2021**, *1016*, 1485–1491. [[CrossRef](#)]
147. Fava, A.; Montanari, R.; Varone, A. Mechanical spectroscopy investigation of point defect-driven phenomena in a Cr martensitic steel. *Metals* **2018**, *8*, 870. [[CrossRef](#)]
148. Montanari, R.; Varone, A. Synergic Role of Self-interstitials and Vacancies in Indium Melting. *Metals* **2015**, *5*, 1061–1072. [[CrossRef](#)]
149. Balijepalli, S.K.; Donnini, R.; Kaciulis, S.; Lucci, M.; Montanari, R.; Ucciardello, N.; Varone, A. Modulo elastico della fase S in un acciaio 316 L kolsterizzato. *La Metall. Ital.* **2013**, *105*, 42–47.
150. Balijepalli, S.K.; Donnini, R.; Kaciulis, S.; Montanari, R.; Varone, A. Young's modulus profile in kolsterized AISI 316 L steel. *Mater. Sci. Forum* **2013**, *762*, 183–188. [[CrossRef](#)]
151. Montanari, R.; Varone, A. Mechanical spectroscopy investigation of liquid Pb-Bi alloys. *Solid State Phenom.* **2012**, *184*, 434–439. [[CrossRef](#)]
152. Hadadzadeh, A.; Baxter, C.; Amirkhiz, B.S.; Mohammadi, M. Strengthening Mechanisms in Direct Metal Laser Sintered AlSi10Mg: Comparison between Virgin and Recycled Powders. *Addit. Manuf.* **2018**, *23*, 108–120. [[CrossRef](#)]
153. Mohammadpour, P.; Plotkowski, A.; Phillion, A.B. Revisiting Solidification Microstructure Selection Maps in the Frame of Additive Manufacturing. *Addit. Manuf.* **2020**, *31*, 100936. [[CrossRef](#)]
154. Li, S.; Zhang, L.-J.; Ning, J.; Wang, X.; Zhang, G.-F.; Zhang, J.-X.; Na, S.-J.; Fatemeh, B. Comparative Study on the Microstructures and Properties of Wire+arc Additively Manufactured 5356 Aluminium Alloy with Argon and Nitrogen as the Shielding Gas. *Addit. Manuf.* **2020**, *34*, 101206. [[CrossRef](#)]

155. Bian, H.; Aoyagi, K.; Zhao, Y.; Maeda, C.; Mouri, T.; Chiba, A. Microstructure Refinement for Superior Ductility of Al–Si Alloy by Electron Beam Melting. *Addit. Manuf.* **2020**, *32*, 100982. [[CrossRef](#)]
156. Aversa, A.; Lorusso, M.; Trevisan, F.; Ambrosio, E.P.; Calignano, F.; Manfredi, D.; Biamino, S.; Fino, P.; Lombardi, M.; Pavese, M. Effect of Process and Post-Process Conditions on the Mechanical Properties of an A357 Alloy Produced via Laser Powder Bed Fusion. *Metals* **2017**, *7*, 68. [[CrossRef](#)]
157. Hooper, P.A. Melt Pool Temperature and Cooling Rates in Laser Powder Bed Fusion. *Addit. Manuf.* **2018**, *22*, 548–559. [[CrossRef](#)]
158. Brandl, E.; Heckenberger, U.; Holzinger, V.; Buchbinder, D. Additive Manufactured AlSi10Mg Samples Using Selective Laser Melting (SLM): Microstructure, High Cycle Fatigue, and Fracture Behavior. *Mater. Des.* **2012**, *34*, 159–169. [[CrossRef](#)]
159. Ghasemi, A.; Fereiduni, E.; Balbaa, M.; Jadhav, S.D.; Elbestawi, M.; Habibi, S. Influence of Alloying Elements on Laser Powder Bed Fusion Processability of Aluminum: A New Insight into the Oxidation Tendency. *Addit. Manuf.* **2021**, *46*, 102145. [[CrossRef](#)]
160. Mauduit, A. Study of the Suitability of Aluminum Alloys for Additive Manufacturing by Laser Powder Bed Fusion. *UPB Sci. Bull. Ser. B Chem. Mater. Sci.* **2017**, *79*, 219–238.
161. Karg, M.; Ahuja, B.; Kuryntsev, S.; Gorunov, A.; Schmidt, M. Processability of High Strength Aluminium-Copper Alloys AW-2022 and 2024 by Laser Beam Melting in Powder Bed. In Proceedings of the 25th Annual International Solid Freeform Fabrication (SFF) Symposium—An Additive Manufacturing Conference, Austin, TX, USA, 4–6 August 2014.
162. Sun, S.; Zheng, L.; Liu, Y.; Liu, J.; Zhang, H. Characterization of Al–Fe–V–Si Heat-Resistant Aluminum Alloy Components Fabricated by Selective Laser Melting. *J. Mater. Res.* **2015**, *30*, 1661–1669. [[CrossRef](#)]
163. Jia, Q.; Rometsch, P.; Kürsteiner, P.; Chao, Q.; Huang, A.; Weyland, M.; Bourgeois, L.; Wu, X. Selective laser melting of a high strength Al–Mn–Sc alloy: Alloy design and strengthening mechanisms. *Acta Mater.* **2019**, *171*, 108–118. [[CrossRef](#)]
164. Zhang, H.; Gu, D.; Yang, J.; Dai, D.; Zhao, T.; Hong, C.; Gasser, A.; Poprawe, R. Selective Laser Melting of Rare Earth Element Sc Modified Aluminum Alloy: Thermodynamics of Precipitation Behavior and Its Influence on Mechanical Properties. *Addit. Manuf.* **2018**, *23*, 1–12. [[CrossRef](#)]
165. Agrawal, P.; Gupta, S.; Thapliyal, S.; Shukla, S.; Haridas, R.S.; Mishra, R.S. Additively manufactured novel Al–Cu–Sc–Zr alloy: Microstructure and mechanical properties. *Addit. Manuf.* **2021**, *37*, 101623. [[CrossRef](#)]
166. Glerum, J.A.; Kenel, C.; Sun, T.; Dunand, D.C. Synthesis of Precipitation-Strengthened Al–Sc, Al–Zr and Al–Sc–Zr Alloys via Selective Laser Melting of Elemental Powder Blends. *Addit. Manuf.* **2020**, *36*, 101461. [[CrossRef](#)]
167. Opprecht, M.; Garandet, J.-P.; Roux, G.; Flament, C.; Soulier, M. A Solution to the Hot Cracking Problem for Aluminium Alloys Manufactured by Laser Beam Melting. *Acta Mater.* **2020**, *197*, 40–53. [[CrossRef](#)]
168. Liu, X.; Liu, Y.; Zhou, Z.; Wang, K.; Zhan, Q.; Xiao, X. Grain Refinement and Crack Inhibition of Selective Laser Melted AA2024 Aluminum Alloy via Inoculation with TiC–TiH₂. *Mater. Sci. Eng. A* **2021**, *813*, 141171. [[CrossRef](#)]
169. Mair, P.; Goettgens, V.S.; Rainer, T.; Weinberger, N.; Letofsky-Papst, I.; Mitsche, S.; Leichtfried, G. Laser Powder Bed Fusion of Nano–CaB₆ Decorated 2024 Aluminum Alloy. *J. Alloys Compd.* **2021**, *863*, 158714. [[CrossRef](#)]
170. Zhou, L.; Hyer, H.; Chang, J.; Mehta, A.; Huynh, T.; Yang, Y.; Sohn, Y. Microstructure, Mechanical Performance, and Corrosion Behavior of Additively Manufactured Aluminum Alloy 5083 with 0.7 and 1.0 Wt% Zr Addition. *Mater. Sci. Eng. A* **2021**, *823*, 141679. [[CrossRef](#)]
171. Tan, Q.; Zhang, J.; Sun, Q.; Fan, Z.; Li, G.; Yin, Y.; Liu, Y.; Zhang, M.-X. Inoculation Treatment of an Additively Manufactured 2024 Aluminium Alloy with Titanium Nanoparticles. *Acta Mater.* **2020**, *196*, 1–16. [[CrossRef](#)]
172. Otani, Y.; Sasaki, S. Effects of the Addition of Silicon to 7075 Aluminum Alloy on Microstructure, Mechanical Properties, and Selective Laser Melting Processability. *Mater. Sci. Eng. A* **2020**, *777*, 139079. [[CrossRef](#)]
173. Zhou, S.Y.; Su, Y.; Wang, H.; Enz, J.; Ebel, T.; Yan, M. Selective Laser Melting Additive Manufacturing of 7xxx Series Al–Zn–Mg–Cu Alloy: Cracking Elimination by Co-Incorporation of Si and TiB₂. *Addit. Manuf.* **2020**, *36*, 101458. [[CrossRef](#)]
174. Qi, Y.; Hu, Z.; Zhang, H.; Nie, X.; Zhang, C.; Zhu, H. High Strength Al–Li Alloy Development for Laser Powder Bed Fusion. *Addit. Manuf.* **2021**, *47*, 102249. [[CrossRef](#)]
175. Belelli, F.; Casati, R.; Vedani, M. Development of Al–Cu–Mg and Al–Mg–Si–Zr Alloys with Improved L-PBF Processability. In Proceedings of the 151st Annual Meeting and Exhibition of The Minerals, Metals and Materials Society, TMS 2022, Anaheim, CA, USA, 27 February–3 March 2022; pp. 289–297. [[CrossRef](#)]
176. Belelli, F.; Casati, R.; Vedani, M. Effect of Cu Content on Hot-Crack Resistance of Al–Cu–Mg Alloys Produced by Laser Powder Bed Fusion. *Philos. Mag. Lett.* **2022**, *102*, 111–119. [[CrossRef](#)]
177. Casati, R.; Coduri, M.; Riccio, M.; Rizzi, A.; Vedani, M. Development of a High Strength Al–Zn–Si–Mg–Cu Alloy for Selective Laser Melting. *J. Alloys Compd.* **2019**, *801*, 243–253. [[CrossRef](#)]
178. Marola, S.; Gianoglio, D.; Bosio, F.; Aversa, A.; Lorusso, M.; Manfredi, D.; Lombardi, M.; Battezzati, L. Alloying AlSi10Mg and Cu Powders in Laser Single Scan Tracks, Melt Spinning, and Laser Powder Bed Fusion. *J. Alloys Compd.* **2020**, *821*, 153538. [[CrossRef](#)]
179. Belelli, F.; Casati, R.; Vedani, M.; Volpp, J. Design and Characterization of Al–Mg–Si–Zr Alloys with Improved Laser Powder Bed Fusion Processability. *Metall. Mater. Trans. A* **2022**, *53*, 331–343. [[CrossRef](#)]
180. Wang, Z.; Lin, X.; Kang, N.; Hu, Y.; Chen, J.; Huang, W. Strength–Ductility Synergy of Selective Laser Melted Al–Mg–Sc–Zr Alloy with a Heterogeneous Grain Structure. *Addit. Manuf.* **2020**, *34*, 101260. [[CrossRef](#)]
181. Zhang, J.; Gao, J.; Song, B.; Zhang, L.; Han, C.; Cai, C.; Zhou, K.; Shi, Y. A Novel Crack-Free Ti-Modified Al–Cu–Mg Alloy Designed for Selective Laser Melting. *Addit. Manuf.* **2021**, *38*, 101829. [[CrossRef](#)]

182. Goebel, J.; Ghidini, T.; Graham, A.J. Stress-Corrosion Cracking Characterisation of the Advanced Aerospace Al–Li 2099-T86 Alloy. *Mater. Sci. Eng. A* **2016**, *673*, 16–23. [[CrossRef](#)]
183. Chen, R.; Wang, H.; He, B.; Tu, Y.; Tang, H. Effect of Thermal Cycling on Microstructure and Mechanical Properties of 2A97 Al–Li Alloy Fabricated by Direct Laser Deposition. *Vacuum* **2021**, *190*, 110299. [[CrossRef](#)]
184. Yürekli, B.; Schade, L.; Ullsperger, T.; Seyfarth, B.; Kohl, H.; Matthäus, G.; Liu, D.; Rettenmayr, M.; Nolte, S. Additive Manufacturing of Binary Al–Li Alloys. *Procedia CIRP* **2020**, *94*, 69–73. [[CrossRef](#)]
185. Li, L.; Meng, X.; Huang, S.; Wang, H.; Li, P.; Zhou, J. Investigating the Effect of the Scanning Speed on the Characteristics of Al–Li Alloy Fabricated by Selective Laser Melting. *J. Manuf. Process.* **2022**, *75*, 719–728. [[CrossRef](#)]
186. Bahl, S.; Sisco, K.; Yang, Y.; Theska, F.; Primig, S.; Allard, L.F.; Michi, R.A.; Fancher, C.; Stump, B.; Dehoff, R.; et al. Al–Cu–Ce(–Zr) Alloys with an Exceptional Combination of Additive Processability and Mechanical Properties. *Addit. Manuf.* **2021**, *48*, 102404. [[CrossRef](#)]
187. Czerwinski, F. Cerium in Aluminum Alloys. *J. Mater. Sci.* **2020**, *55*, 24–72. [[CrossRef](#)]
188. Czerwinski, F. Thermal Stability of Aluminum Alloys. *Materials* **2020**, *13*, 3441. [[CrossRef](#)]
189. Czerwinski, F. Critical Assessment 40: A Search for the Eutectic System of High-Temperature Cast Aluminium Alloys. *Mater. Sci. Technol.* **2021**, *37*, 683–692. [[CrossRef](#)]
190. Czerwinski, F. Thermal Stability of Aluminum–Cerium Binary Alloys Containing the Al–Al₁₁Ce₃ Eutectic. *Mater. Sci. Eng. A* **2021**, *809*, 140973. [[CrossRef](#)]
191. Ng, D.S.; Dunand, D.C. Aging- and creep-resistance of a cast hypoeutectic Al–6.9Ce–9.3Mg (wt%) alloy. *Mater. Sci. Eng. A* **2020**, *786*, 139398. [[CrossRef](#)]
192. Plotkowski, A.; Sisco, K.; Bahl, S.; Shyam, A.; Yang, Y.; Allard, L.; Nandwana, P.; Rossy, A.M.; Dehoff, R.R. Microstructure and Properties of a High Temperature Al–Ce–Mn Alloy Produced by Additive Manufacturing. *Acta Mater.* **2020**, *196*, 595–608. [[CrossRef](#)]
193. Manca, D.R.; Churyumov, A.Y.; Pozdniakov, A.V.; Prosviryakov, A.S.; Ryabov, D.K.; Krokhin, A.Y.; Korolev, V.A.; Daubarayte, D.K. Microstructure and Properties of Novel Heat Resistant Al–Ce–Cu Alloy for Additive Manufacturing. *Met. Mater. Int.* **2019**, *25*, 633–640. [[CrossRef](#)]
194. Yang, Y.; Bahl, S.; Sisco, K.; Lance, M.; Shin, D.; Shyam, A.; Plotkowski, A.; Dehoff, R.R. Primary Solidification of Ternary Compounds in Al–Rich Al–Ce–Mn Alloys. *J. Alloys Compd.* **2020**, *844*, 156048. [[CrossRef](#)]
195. Zhou, L.; Huynh, T.; Park, S.; Hyer, H.; Mehta, A.; Song, S.; Bai, Y. Laser powder bed fusion of Al–10 wt% Ce alloys: Microstructure and tensile property. *J. Mater. Sci.* **2020**, *55*, 14611–14625. [[CrossRef](#)]
196. Dantzig, J.A.; Rappaz, M. *Solidification: Revised & Expanded*; EPFL Press: Lausanne, Switzerland, 2016.
197. Tiwary, C.S.; Pandey, P.; Sarkar, S.; Das, R.; Samal, S.; Biswas, K.; Chattopadhyay, K. Five Decades of Research on the Development of Eutectic as Engineering Materials. *Prog. Mater. Sci.* **2022**, *123*, 100793. [[CrossRef](#)]
198. Knipling, K.E.; Dunand, D.C.; Seidman, D.N. Criteria for Developing Castable, Creep-Resistant Aluminum-Based Alloys—A Review. *Int. J. Mater. Res.* **2006**, *97*, 246–265. [[CrossRef](#)]
199. Prashanth, K.G.; Shahabi, H.S.; Attar, H.; Srivastava, V.C.; Ellendt, N.; Uhlenwinkel, V.; Eckert, J.; Scudino, S. Production of High Strength Al₈₅Nd₈Ni₅Co₂ Alloy by Selective Laser Melting. *Addit. Manuf.* **2015**, *6*, 1–5. [[CrossRef](#)]
200. Thapliyal, S.; Shukla, S.; Zhou, L.; Hyer, H.; Agrawal, P.; Agrawal, P.; Komarasamy, M.; Sohn, Y.; Mishra, R.S. Design of Heterogeneous Structured Al Alloys with Wide Processing Window for Laser-Powder Bed Fusion Additive Manufacturing. *Addit. Manuf.* **2021**, *42*, 102002. [[CrossRef](#)]
201. Aversa, A.; Bosio, F.; Marola, S.; Lorusso, M.; Manfredi, D.; Battezzati, L.; Fino, P.; Lombardi, M. Laser single scan tracks of new aluminium alloys compositions. In Proceedings of the Euro PM 2018 Congress and Exhibition, Bilbao, Spain, 14–18 October 2020.
202. Belevi, F.; Casati, R.; Larini, F.; Riccio, M.; Vedani, M. Investigation on Two Ti–B-Reinforced Al Alloys for Laser Powder Bed Fusion. *Mater. Sci. Eng. A* **2021**, *808*, 140944. [[CrossRef](#)]
203. Li, W.; Li, S.; Liu, J.; Zhang, A.; Zhou, Y.; Wei, Q.; Yan, C.; Shi, Y. Effect of Heat Treatment on AlSi10Mg Alloy Fabricated by Selective Laser Melting: Microstructure Evolution, Mechanical Properties and Fracture Mechanism. *Mater. Sci. Eng. A* **2016**, *663*, 116–125. [[CrossRef](#)]
204. Yu, Y.; Kenevisi, M.S.; Yan, W.; Lin, F. Modeling Precipitation Process of Al–Cu Alloy in Electron Beam Selective Melting with a 3D Cellular Automaton Model. *Addit. Manuf.* **2020**, *36*, 101423. [[CrossRef](#)]
205. Paoletti, C.; Cerri, E.; Ghio, E.; Santecchia, E.; Cabibbo, M.; Spigarelli, S. Effect of Low-Temperature Annealing on Creep Properties of AlSi10Mg Alloy Produced by Additive Manufacturing: Experiments and Modeling. *Metals* **2021**, *11*, 179. [[CrossRef](#)]
206. Hu, Z.; Qi, Y.; Gao, S.; Nie, X.; Zhang, H.; Zhu, H.; Zeng, X. Aging Responses of an Al–Cu Alloy Fabricated by Selective Laser Melting. *Addit. Manuf.* **2021**, *37*, 101635. [[CrossRef](#)]
207. Rao, J.H.; Zhang, Y.; Zhang, K.; Huang, A.; Davies, C.H.J.; Wu, X. Multiple Precipitation Pathways in an Al–7Si–0.6Mg Alloy Fabricated by Selective Laser Melting. *Scr. Mater.* **2019**, *160*, 66–69. [[CrossRef](#)]
208. Tang, M.; Pistorius, P.C. Oxides, Porosity and Fatigue Performance of AlSi10Mg Parts Produced by Selective Laser Melting. *Int. J. Fatigue* **2017**, *94*, 192–201. [[CrossRef](#)]
209. Nicoletto, G. Influence of rough as-built surfaces on smooth and notched fatigue behavior of L-PBF AlSi10Mg. *Addit. Manuf.* **2020**, *34*, 101251. [[CrossRef](#)]

210. Uzan, N.E.; Ramati, S.; Shneck, R.; Frage, N.; Yeheskel, O. On the Effect of Shot-Peening on Fatigue Resistance of AlSi10Mg Specimens Fabricated by Additive Manufacturing Using Selective Laser Melting (AM-SLM). *Addit. Manuf.* **2018**, *21*, 458–464. [[CrossRef](#)]
211. Uzan, N.E.; Shneck, R.; Yeheskel, O.; Frage, N. Fatigue of AlSi10Mg Specimens Fabricated by Additive Manufacturing Selective Laser Melting (AM-SLM). *Mater. Sci. Eng. A* **2017**, *704*, 229–237. [[CrossRef](#)]
212. Tradowsky, U.; White, J.; Ward, R.M.; Read, N.; Reimers, W.; Attallah, M.M. Selective Laser Melting of AlSi10Mg: Influence of Post-Processing on the Microstructural and Tensile Properties Development. *Mater. Des.* **2016**, *105*, 212–222. [[CrossRef](#)]
213. Giovagnoli, M.; Tocci, M.; Fortini, A.; Merlin, M.; Ferroni, M.; Migliori, A.; Pola, A. Effect of Different Heat-Treatment Routes on the Impact Properties of an Additively Manufactured AlSi10Mg Alloy. *Mater. Sci. Eng. A* **2021**, *802*, 140671. [[CrossRef](#)]
214. Di Egidio, G.; Ceschini, L.; Morri, A.; Martini, C.; Merlin, M. A Novel T6 Rapid Heat Treatment for AlSi10Mg Alloy Produced by Laser-Based Powder Bed Fusion: Comparison with T5 and Conventional T6 Heat Treatments. *Metall. Mater. Trans. B* **2022**, *53*, 284–303. [[CrossRef](#)]
215. Schneller, W.; Leitner, M.; Leuders, S.; Sprauel, J.M.; Grün, F.; Pfeifer, T.; Jantschner, O. Fatigue Strength Estimation Methodology of Additively Manufactured Metallic Bulk Material. *Addit. Manuf.* **2021**, *39*, 101688. [[CrossRef](#)]
216. Murakami, Y. *Metal Fatigue: Effects of Small Defects and Nonmetallic Inclusions*; Academic Press: London, UK, 2019.

Disclaimer/Publisher’s Note: The statements, opinions and data contained in all publications are solely those of the individual author(s) and contributor(s) and not of MDPI and/or the editor(s). MDPI and/or the editor(s) disclaim responsibility for any injury to people or property resulting from any ideas, methods, instructions or products referred to in the content.